Recent Surface Rupturing Earthquakes along the South Flank of the Greater Caucasus near Tbilisi, Georgia

Timothy A. Stahl*¹, Eric Cowgill², Giorgi Boichenko³, Dylan A. Vasey², and Tea Godoladze³

ABSTRACT

Fault characterization is a critical step toward improving seismic hazard assessment in the Georgian Greater Caucasus but is largely absent from the region. Here, a paleoseismic trench near the capital city of Tbilisi revealed evidence for recurring surface rupture on a shallowly north-dipping thrust fault. The fault has broken through the overturned forelimb of a fault-propagation anticline that folds a sequence of soils and deposits. Stratigraphic relationships and radiocarbon dating of terrestrial gastropod shells corrected for "old carbon" age anomalies loosely constrain three surface-deforming earthquakes on this fault between ~ 40 and ~ 3 ka, with variable dip-slip displacements ranging between 0.35 and ~ 3 m, and a cumulative displacement of 6.5 \pm 0.85 m. Single event slips and recurrence intervals (11, 25, and 3 ka open interval) at this site demonstrate apparent slip rate variations of 3–7 \times over the last two earthquake cycles on the fault, which we attribute to possible rupture complexity involved in crustal thrust fault earthquakes. This study provides a structural and geochronologic template for future paleoseismic investigations in the Greater Caucasus while highlighting some of the challenges of conducting seismic source characterization in this region.

KEY POINTS

- We present paleoseismic evidence for surface rupturing earthquakes in the Greater Caucasus.
- Trenching revealed a gently dipping thrust with evidence for three events over the last ~40 ka.
- Further seismic source characterization is required, particularly near the capital city of Tbilisi.

Supplemental Material

INTRODUCTION

Fault characterization is an important component of understanding both regional tectonics and seismic hazard. In the central Greater Caucasus of Georgia, the Arabian and Eurasian plates converge at orogen-perpendicular rates of between 2 and 14 mm yr⁻¹ (Reilinger *et al.*, 2006; Forte *et al.*, 2013; Sokhadze *et al.*, 2018), resulting in a series of folds cored by northeast- and southwest-vergent thrust faults (Dotduyev, 1986; Banks *et al.*, 1997; Adamia *et al.*, 2010, 2017; Forte *et al.*, 2010, 2013; Nemčok *et al.*, 2013; Alania *et al.*, 2017, 2021). However, only a few studies have been published regarding the displacement histories, geologically derived slip rates, and potential magnitudes of surface rupturing earthquakes on faults in this region (Khromovskikh *et al.*, 1979;

Rogozhin *et al.*, 2002; Rogozhin *et al.*, 2004, and references therein), leading to uncertainty in (1) where and how plate convergence is accommodated over late Pleistocene timescales and (2) where seismic hazard is presently the greatest (Onur *et al.*, 2020). These are salient issues near Tbilisi (population 1.5 million), the capital of Georgia, where elastic-dislocation modeling of Global Positioning System (GPS) velocities indicates that maximum plate-normal strain is located within about 20 km of the city (Sokhadze *et al.*, 2018), but the active structures accommodating this strain remain unidentified.

Near Tbilisi, GPS data indicate that convergence between the Lesser and Greater Caucasus is predominantly accommodated within the foreland Kartli and Kura basins, although it remains unclear whether this shortening is localized on a south-dipping fault beneath the Lesser Caucasus, a north-dipping fault beneath the Greater Caucasus, or both (Sokhadze

^{1.} School of Earth and Environment, University of Canterbury, Christchurch, New Zealand, https://orcid.org/0000-0003-3016-7322 (TAS); 2. Department of Earth and Planetary Sciences, University of California, Davis, California, U.S.A., https://orcid.org/0000-0001-6017-4748 (EC); https://orcid.org/0000-0002-2182-4733 (DAV); 3. Institute of Earth Sciences, Ilia State University, Tbilisi, Georgia

^{*}Corresponding author: timothy.stahl@canterbury.ac.nz

Cite this article as Stahl, T. A., E. Cowgill, G. Boichenko, D. A. Vasey, and T. Godoladze (2022). Recent Surface Rupturing Earthquakes along the South Flank of the Greater Caucasus near Tbilisi, Georgia, *Bull. Seismol. Soc. Am.* 112, 2170–2188, doi: 10.1785/0120210267

[©] Seismological Society of America

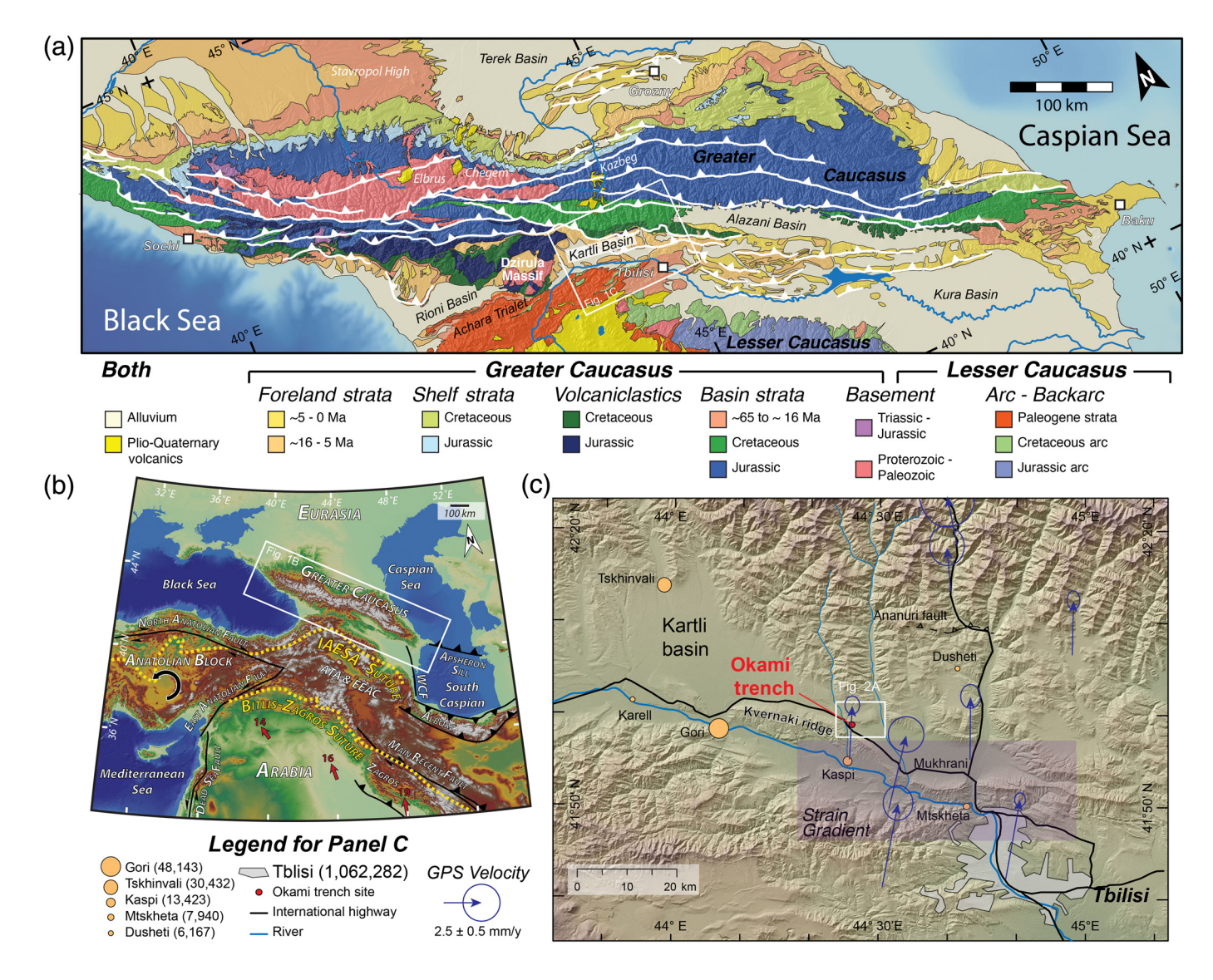


Figure 1. Maps showing the location of the Okami trench site in the context of the Caucasus and Arabia-Eurasia collision. (a) Simplified geologic map of the Caucasus region (modified from Forte et al., 2014). The white lines show a compilation of major faults in the Greater Caucasus (modified from Trexler et al., 2022). The Greater and Lesser Caucasus mountains are separated by the Rioni, Kartli, and Alazani piggyback basins and the Kura foreland basin. Northern margin of the Lesser Caucasus mountains is defined by late Cenozoic faults west of 45° E (Banks et al., 1997; Tari et al., 2018), with no evidence of such deformation to the east. DM indicates Dzirula massif; the Devonian to Triassic Dizi metasedimentary series is lumped with the Proterozoic-Paleozoic basement for simplicity. (b) Overview of the Arabia–Eurasia collision (modified from Cowgill et al., 2016). The black lines denote major structural systems, the red arrows indicate direction and rate (mm/yr) of motion of Arabia relative to Eurasia from the 2010 GEODVEL model (Argus et al., 2010). Abbreviations: ATA, Anatolide-Tauride-Armenian block; EEAC, east Anatolian accretionary

complex; IAESA, Izmir-Ankara-Erzincan-Sevan-Akera; WCF, west Caspian fault. The yellow-dashed lines are the IAESA and Bitlis-Zagros sutures. (c) Shaded relief map showing the location of the Okami paleoseismic trench within the Kartli basin at the west end of the Mukhrani plain (hillshade from Shuttle Radar Topography Mission 30 [SRTM30] topographic data). The blue arrows and shaded box indicate Global Positioning System (GPS) velocities and strain gradient between the Lesser and Greater Caucasus (from Sokhadze et al., 2018); arrows and uncertainty ellipses are scaled to reference velocity shown in legend. The black barbed line indicates trace of Anauri fault from Trexler et al. (2022). The gray polygon indicates outline of Tbilisi, the capital city of Georgia. The orange dots indicate other cities and towns, with numbers in parentheses indicating populations; populations are from census by the State Department for Statistics of Georgia. Highway data originally from DIVA-GIS, adjusted using the topographic data and Google Maps (see Data and Resources). The color version of this figure is available only in the electronic edition.

et al., 2018; Fig. 1). Interpretations of fault geometry in the Kura and Kartli basins have relied on active seismicity, seismic reflection profiles, and mapping of Mesozoic–Tertiary bedrock

relationships (Banks et al., 1997; Adamia et al., 2010, 2017; Forte et al., 2010, 2013; Nemčok et al., 2013; Alania et al., 2017, 2021) (Fig. 1). Few studies have documented deformed

Quaternary landforms or sediments, and the majority of these are in the western Rioni basin (e.g., Tsereteli *et al.*, 2016; Tibaldi, Alania, *et al.*, 2017; Tibaldi, Russo, *et al.*, 2017; Trexler *et al.*, 2020) or the eastern Kura basins (e.g., Forte *et al.*, 2010, 2013; Fig. 1). The largest earthquake in the Greater Caucasus region during the instrumental period did not produce identifiable surface rupture (1991 $M_{\rm s}7.0/M_{\rm w}$ 6.9 Racha earthquake: Jibson *et al.*, 1994; Triep *et al.*, 1995), demonstrating the challenge and utility of characterizing active faults in the area.

In this study, we present the results of a paleoseismic trench investigation across an active thrust fault 40 km northwest of Tbilisi and within about 20 km of the GPS-derived "high-strain" zone reported by Sokhadze *et al.* (2018). Our objectives were to characterize the late Pleistocene to recent record of faulting and to document the relationship of surface deformation with the underlying fault geometry and kinematics.

GEOLOGIC SETTING

Geology of the Greater Caucasus region

The Caucasus region spans all of Georgia and Azerbaijan, as well as portions of Russia, Turkey, and Armenia, and defines the northern margin of the Arabia–Eurasia collision zone between the Black and Caspian seas (Fig. 1). The region is bounded by the Greater and Lesser Caucasus mountains to the north and south, respectively, which are separated by a series of intermontane depressions including the Rioni, Kartli, Alazani, and Kura basins (Adamia *et al.*, 1977; Gamkrelidze, 1986; Fig. 1). The Rioni and Kartli basins are separated along strike by the Dzirula massif, across which the Greater and Lesser Caucasus are topographically connected with no intervening active foreland basin. The axial Mtkvari-Kura river drains most of the intermontane basin region, flowing generally west to east through the Kartli and Kura basins and into the south Caspian basin (Fig. 1).

Structurally, the Greater Caucasus mountains comprise a south-vergent orogenic wedge that is singly vergent at the western and eastern ends of the range and bivergent in the center (Forte et al., 2014). Seismicity (e.g., Jackson, 1992), GPS (e.g., Reilinger et al., 2006; Sokhadze et al., 2018), and geologic (e.g., Forte et al., 2010) data all indicate that, between the Black and Caspian seas, most orogen-perpendicular convergence between the Arabian and Eurasian plates is localized in the Greater Caucasus (Forte et al., 2013). An apparently north-dipping zone of subcrustal earthquakes extends to up to 160 km depth beneath the eastern Greater Caucasus in Azerbaijan and has been interpreted as evidence of northward subduction of Kura basin crust beneath the Greater Caucasus (e.g., Mellors et al., 2012; Mumladze et al., 2015; McKenzie et al., 2019; Gunnels et al., 2020).

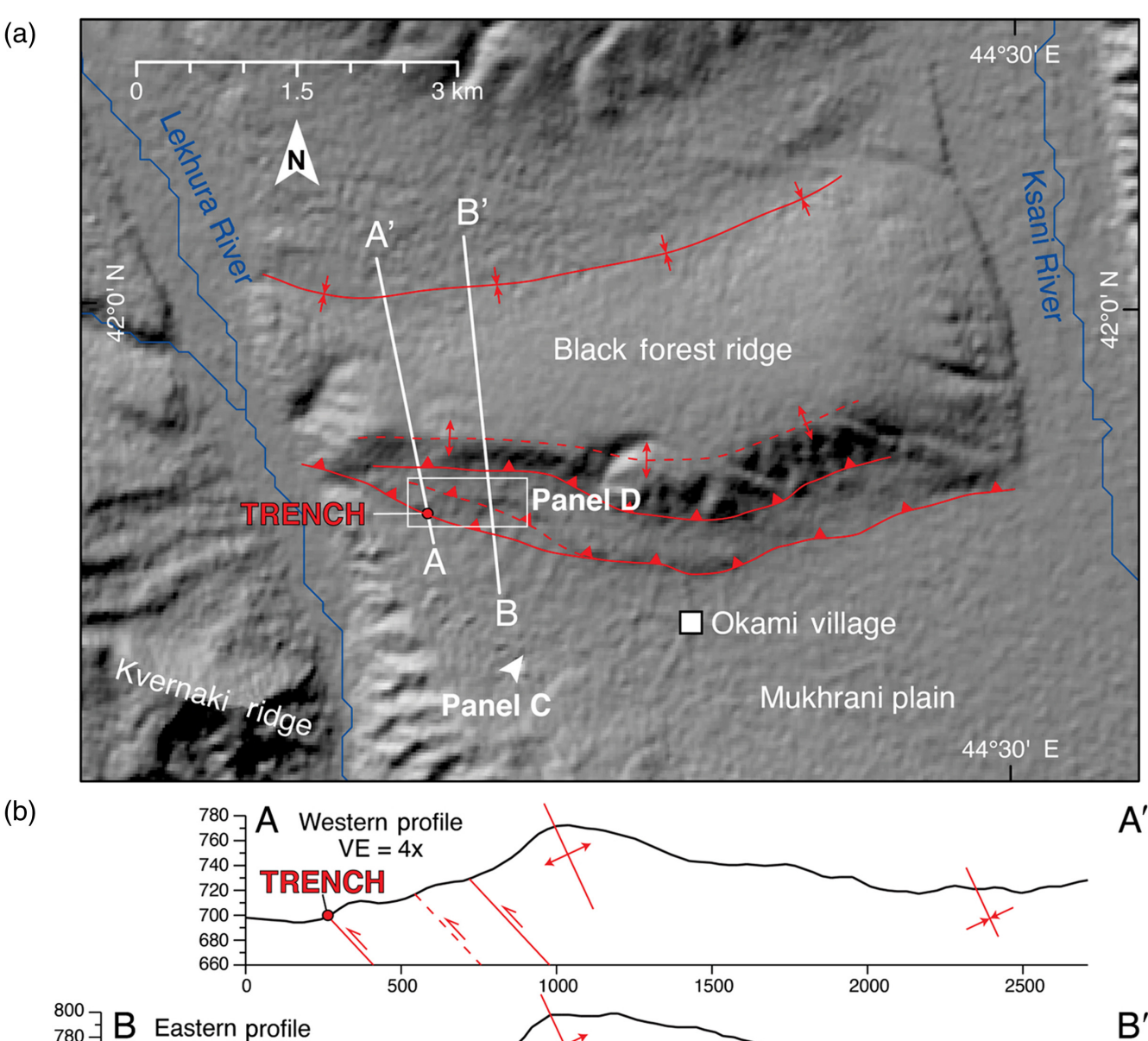
The Caucasus orogen formed by Cenozoic closure of a marine back-arc basin that had opened by middle Jurassic time (~170 Ma) via rifting of the Lesser Caucasus volcanic arc from

the southern margin of Eurasia (e.g., Adamia et al., 1977; Gamkrelidze, 1986; Cowgill et al., 2016; Vasey et al., 2021, and references therein). The intervening basin was analogous to the Black Sea and south Caspian basin, to which it was originally connected (Zonenshain and Le Pichon, 1986; Cowgill et al., 2016), although a basin of such width is disputed (Cowgill et al., 2018; Vincent et al., 2018). Closure of the basin initiated in late Eocene to Oligocene time, as indicated by thermochronologic (Avdeev and Niemi, 2011) and provenance data (Cowgill et al., 2016; Tye et al., 2021), eventually resulting in late Miocene (~5-10 Ma) collision of the Lesser Caucasus arc with the Proterozoic to Paleozoic basement and overlying Paleozoic to Cenozoic sedimentary cover of the Greater Caucasus (Avdeev and Niemi, 2011; Cowgill et al., 2016). Since collision, the locus of active surface shortening has propagated south from the Greater Caucasus into the intervening foreland basins (Forte et al., 2010; Trexler et al., 2020) and is now concentrated in foreland fold-thrust belts in the Rioni, Kartli, and Kura basins. From Tbilisi west to the Black Sea coast, the northern margin of the Lesser Caucasus is deformed by north-directed thrusts and folds within the Achara-Trialet region (Banks et al., 1997; Tari et al., 2018). These structures are post-Eocene and locally as young as late Miocene, but the magnitude and timing of shortening in this belt are poorly known. East of Tbilisi, topographic data, and geologic maps (e.g., Abdullaev, 1962; Shirinov and Bajenov, 1962; Mamedov, 1973; Nalivkin, 1976; Gudjabidze, 2003) provide little evidence of Miocene or younger shortening along the northern margin of the Lesser Caucasus where it bounds the southern margin of the Kura basin (Fig. 1).

Structure and active tectonics of the Kartli basin

The study site is located on an emergent thrust of the Greater Caucasus in the Kartli basin, between the Dzirula massif in the west and Tbilisi in the east (Fig. 2). The structure of the basin is complex here because of the lack of a clear structural separation between the north-dipping thrust system that roots beneath the Greater Caucasus and the south-dipping thrust system that roots beneath the Lesser Caucasus (Banks et al., 1997; Adamia et al., 2010, 2017; Nemčok et al., 2013; Alania et al., 2017, 2021). In detail, the Kartli basin appears to be a wedge-top structural setting (DeCelles, 2012) in which sediments buried the active thrust fronts of the Greater and Lesser Caucasus thrust systems, with no intervening foreland basin underlain by autochthonous strata. These thrust systems have oppositely verging bounding thrusts, and it is possible that they are interacting at depth, as interpreted by Alania et al. (2021), ~17 km east of our study site, although surface observations and published seismic data do not uniquely indicate crosscutting relations.

From north to south, the transition from the Greater to Lesser Caucasus across the Kartli basin comprises a south-directed imbricate stack of thrust sheets carrying upper Cretaceous to



TRENCH
740
780
780
760
740
720
700
680
760
740
720
700
680
660
0
500
1000
1500
2000
2500

B

Company of the second of the second

Figure 2. Location and local structural context of the Okami trench site. (a) Simplified structural map of Black Forest ridge; the red lines indicate structures (dashed where less confident) inferred from topography and poor bedding exposures along the Ksani River; red dot indicates location of Okami trench; hillshade from SRTM30 topographic data. (b) Topographic profiles from SRTM30 topographic data showing secondary ridges along the southern margin of the Black Forest ridge; the red lines indicate structures inferred from topography in panel (a). Topography and structures are both vertically exaggerated (true fault dips are ~15° from trench measurement). Observe local areas of north-sloping topography on southernmost ridge and north of the trench. We interpret this north-sloping area to result from folding and back-tilting of the ground surface above the frontal thrust. See

panel (a) for profile locations. (c) Photograph looking northeast across the Mukhrani plain at the southern margin of Black Forest ridge with secondary ridges in the foreground; sharp horizontal line is an irrigation canal. Singlelane dirt road in distance and cow in foreground for scale. (d) Slope raster and 2 m elevation contours derived from a 1 m digital elevation model produced from field-surveyed Differential Global Positioning System (dGPS) points, which were gridded using standard raster interpolation techniques. The trench site (black rectangle) is located at the base of a south-facing $\sim\!15^\circ$ slope, which was interpreted in the field as the forelimb of an up to $\sim\!18$ m amplitude fold scarp. The color version of this figure is available only in the electronic edition. (Continued)

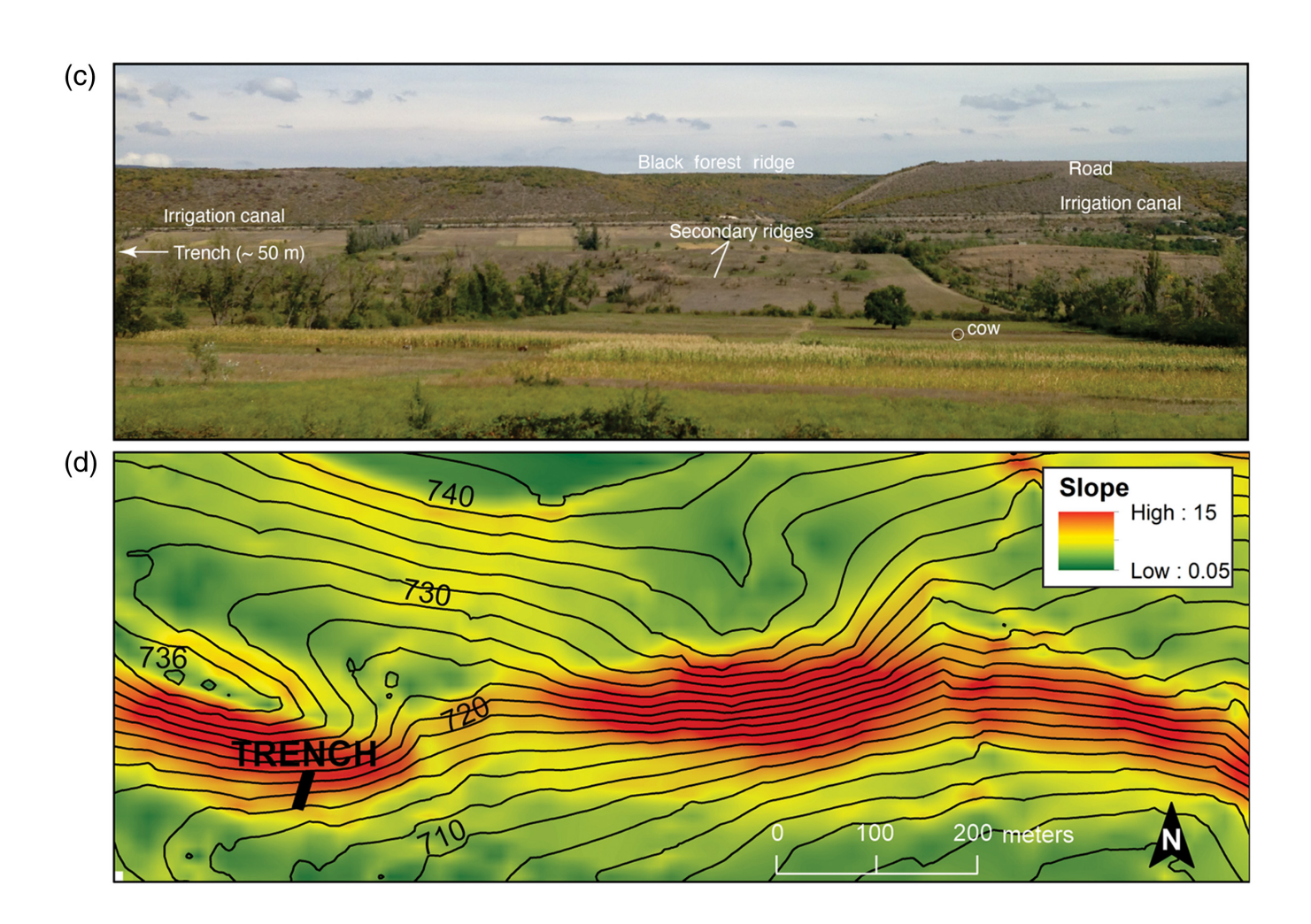


Figure 2. Continued

Paleocene (locally Eocene) strata (Banks et al., 1997; Gudjabidze, 2003; Alania et al., 2017; Trexler et al., 2022) thrust over middle and upper Miocene strata (Sarmatian, Meotian, and Pontian) along the Ananuri fault (Trexler et al., 2022; Fig. 1c). There, upper Miocene (Sarmatian to Pontian) strata, as well as unconformably overlying gravels and geomorphic surfaces of probable Quaternary age, are deformed by south-directed folds (Trexler et al., 2022). In the southern part of the basin, a gently north-dipping homocline above a south-directed thrust exposes an upright section of Oligocene to upper Miocene (Pontian) strata in the Kvernaki ridge (e.g., Banks et al., 1997; Adamia et al., 2010; Alania et al., 2017) (Fig. 1c). The Kvernaki ridge has been interpreted to overlie a triangle zone at the northern tip of a south-dipping thrust system that roots beneath the Lesser Caucasus (Banks et al., 1997; Alania et al., 2017, 2021; Figs. 1, 2). In the structural interpretation of Banks et al. (1997) and Alania et al. (2017), the paleoseismic site described in The Okami Paleoseismic Site section sits on the southernmost emergent thrust within a south-directed thrust system that roots to the north beneath the Greater Caucasus.

GPS data in the Caucasus region and across the Kartli basin provide important constraints on rates and locations of modern deformation. Although geodetic data clearly indicate that strain is localized in the region between the Greater and Lesser Caucasus (e.g., Sokhadze et al., 2018), the locus of this strain appears to vary along strike. To the west (~43.3° E), in the Racha region on the north side of the Dzirula massif (Fig. 1), GPS observations are best matched by a north-dipping elastic dislocation positioned near the southern margin of the Greater Caucasus. Although the data permit a range of locking depths, dislocation dips, and slip rates, the preferred solution is a north-dipping thrust dislocation that strikes 285°, dips 26°, and slips at a rate of 4.2 mm/yr below a locking depth of 10 km (Sokhadze et al., 2018). Important, the locking line along the up-dip edge of this dislocation lies north of the northern margins of the Rioni and Kartli basins (Fig. 1). In contrast, to the east near Tbilisi (44.8° E), the strain field is best matched by a south-dipping thrust dislocation beneath the Lesser Caucasus and south of the Kartli basin, with the preferred solution being a dislocation that strikes 090°, dips 36°, and slips at a rate of

4.2 mm/yr below a locking depth of 16 km (Sokhadze et al., 2018). However, the data on this profile are also adequately fit by a north-dipping dislocation that is beneath the Greater Caucasus and north of the Kartli basin that strikes 270°, dips 36°, and slips at a rate of 4.0 mm/yr below a locking depth of 12 km (Sokhadze et al., 2018). If correct, this latter scenario suggests southward propagation into the Kartli basin of a thrust rooting into the Greater Caucasus to the north. In either case, the position of the modeled locking line relative to the surface expression of active faulting within the Kartli basin seems to indicate that the foreland fold-thrust belt is underlain by a locked basal thrust that has a significant down-dip extent and is being elastically loaded by a creeping dislocation at depth.

The Okami paleoseismic site

General description and analytical methods. We selected a trench site along the southern margin of Black Forest ridge near the Lekhura River and the village of Okami (Fig. 2). The crest of the Black Forest ridge (~750–800 m elevation) separates a gently north-sloping back panel that is ~1.5 km wide across strike from a narrower and more steeply sloping face to the south. In front of the southern face is a secondary ridge that is ~150 m wide across strike and at most ~40 m high relative to the plain to the south. As with the main ridge to the north, slopes are asymmetric across the secondary ridge, with gentle northward slopes into the main ridge on the northern side and steeper southward slopes on the southern side (Fig. 2d). The trench site is located at the base of the southern slope of the secondary ridge.

During site visits, we interpreted this ridge to be formed by a splay of the master fault underlying the Black Forest anticline (Fig. 2). The downthrown side of this splay fault contains a Quaternary alluvial fan of the Lekhura River to the west. We expect the youngest deposits of this fan to be 10^4 – 10^5 yr old, owing to their position about 60 m above modern stream level and assuming incision rates of 0.1–1 mm yr⁻¹. It is unclear whether this fan surface is continuous onto the upthrown side of the secondary ridge, although it seems likely that the site has received some colluvial input from the forelimb of the Black Forest anticline to the north (Fig. 2). Regionally, the land surface has been heavily cultivated, likely for >2000 yr, and humans have inhabited the area for >30,000 yr based on nearby archaeological site chronologies (e.g., Bar-Yosef et al., 2011).

A 25-m-long backhoe excavation across this splay fault revealed evidence of near-surface faulting and folding (Figs. 3, 4). The trench walls were cleaned then gridded with string line at 1×1 m intervals. Photographs of the 1×1 m grids were corrected for lens distortion and orthophotos were printed at 1:5 scale. Field logging took place directly on orthophotos; a photomosaic incorporating our interpretations was constructed after field work. A photogrammetric digital surface

model of the trench walls was constructed using structure from motion after removing the logging grid. The resultant orthomosaic is available in the supplemental material to this article. During logging, we split or lumped depositional and soil-stratigraphic units as needed to identify individual paleoseismic events and refer to all such horizons simply as "units". Because fault-kinematic data presented in the following indicate minimal out-of-plane motion, we measured fault displacement as the dip separation of units along the major fault strands. For simplicity, we used the convention of naming progressively younger units and events with increasing numbers.

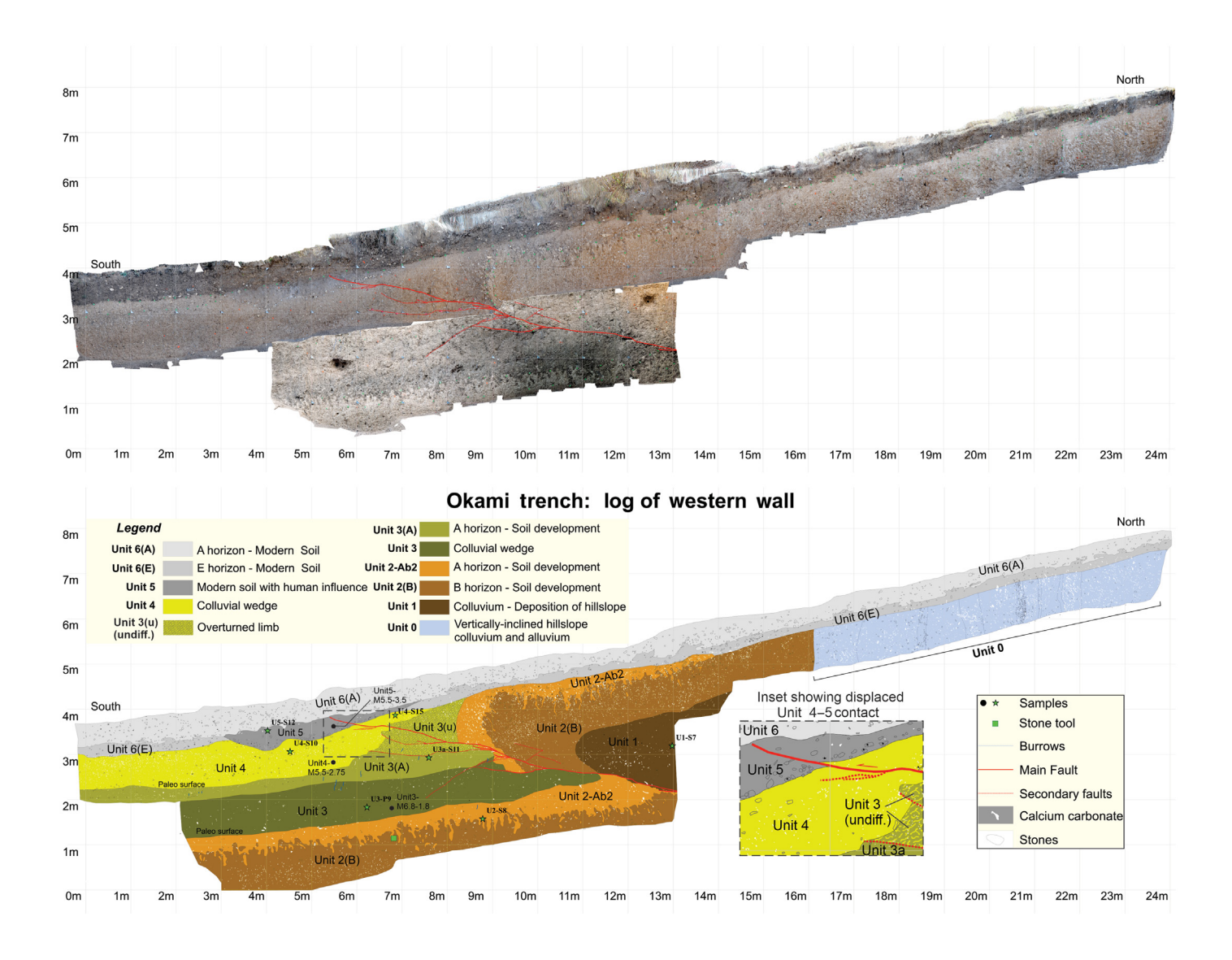
Two types of samples were collected to constrain the ages of trench stratigraphy via accelerator mass spectrometry (AMS): terrestrial gastropods and bulk soil samples for organic material extraction. Gastropod species *Xeropicta derbentina* and *Helix lucorum* were ubiquitous throughout trench stratigraphy and modern environment. Whole and fragmented in situ specimens were collected from trench strata. Samples were sent to the University of California Irvine Keck Carbon Cycle Facility for treatment, measurement of ¹⁴C activity, and AMS dating.

Terrestrial gastropods present some methodological challenges for radiocarbon dating. Some terrestrial species ingest "old" pedogenic carbonate, which is abundant at the trench site, producing taxon-specific radiocarbon age anomalies and radiocarbon dates older than the true age (Goodfriend and Stipp, 1983; Goodfriend, 1987). In some species and terrains, such anomalies can be hundreds to up to 3000 yr (Goodfriend and Stipp, 1983), whereas other, typically smaller, taxa show limited or no evidence for such anomalies (Pigati *et al.*, 2004, 2010). To ensure age reliability, it is important to date and measure the ¹⁴C activity of modern specimens to control for this effect (Pigati *et al.*, 2004, 2010).

We collected modern shells of both species to control for the old carbon problem, although it is important to observe that the effect is not always systematic within a species. We also collected bulk soil samples, from which charcoal was able to be extracted, to assess age variability between sample targets (i.e., gastropods and charcoal). Further detail regarding sample targets and their preparation is included in the supplemental material.

TRENCH STRATIGRAPHY

Strata exposed in trench primarily comprise (1) hillslope colluvium and alluvium, (2) carbonate-rich paleosols and modern soil, and (3) colluvial deposits sourced from erosion of the scarp. Positions on the log are referred to by their horizontal (H) and vertical (V) locations in meters (M) relative to an origin at the south end of the log in the lower left corner (Fig. 3). Full unit descriptions are provided in the supplemental material and Table S1 available in the supplemental material to this article; brief descriptions and interpretations are provided here.



Unit 0 is only observed at the north end of the trench (past meter 16 horizontal, M16H, Fig. 3), where it comprises vertical (85°–90° south-dipping) beds of predominantly silt to silty clay with lesser amounts of sand and gravel (Fig. 3). We interpret these beds as the oldest units exposed in the trench based on stratigraphic relationships and infer that they represent a mixed alluvial and colluvial input from the Lekhura River and the forelimb of the Black Forest anticline, respectively (Fig. 2).

Unit 1 is a massive silty clay with <10% sand- to cobble-size grains and no discernable clast fabric. We interpret unit 1 to be reworked material from unit 0. Unit 2 consists of $CaCO_3$ -rich silty clay that we interpret to be an \sim 1-m-thick buried soil profile developed on unit 1. A possible artifact, a denticulate stone, was found at the base of Ab2 at the south end of the trench (Figs. 3, 5) and extracted for further identification.

Unit 3 is a silty clay limited to the southern half of the trench (up to M11H, Fig. 3) and locally defines a northward-closing wedge of material above unit 2. The unit is similar in most characteristics to underlying unit 2, with the two units being distinguished by a distinct (~2 cm wide) wavy

Figure 3. Trench log. See the supplemental material for A3-size orthophoto of the trench and full unit descriptions. Here and in text, positions on the log are referred to by their horizontal (H) and vertical (V) locations in meters (M) relative to an origin at the south end of the log in the lower left corner.

contact, above which there is a faint stone line and increase in silt content (10%–20%). We interpret unit 3 to be a deposit of colluvial origin in the downthrown side of the fold (discussed subsequently), derived from the erosion and reworking of units 1 and 2. We interpret unit 3a to be a buried A horizon developed on unit 3.

Unit 3 (undiff.) comprises a wedge of material between units 3a and 4 in a part of the trench in which contacts could not be identified confidently. We were unable to subdivide or identify internal structure within unit 3 (undiff.) due to the lack of coherent sedimentary or soil structure within this zone, possibly due to it being within the hinge zone of an interpreted fold at M9H-3.5 V (Fig. 3). However, we are confident that the base of this unit represents the folded contact between units 3 and 2.

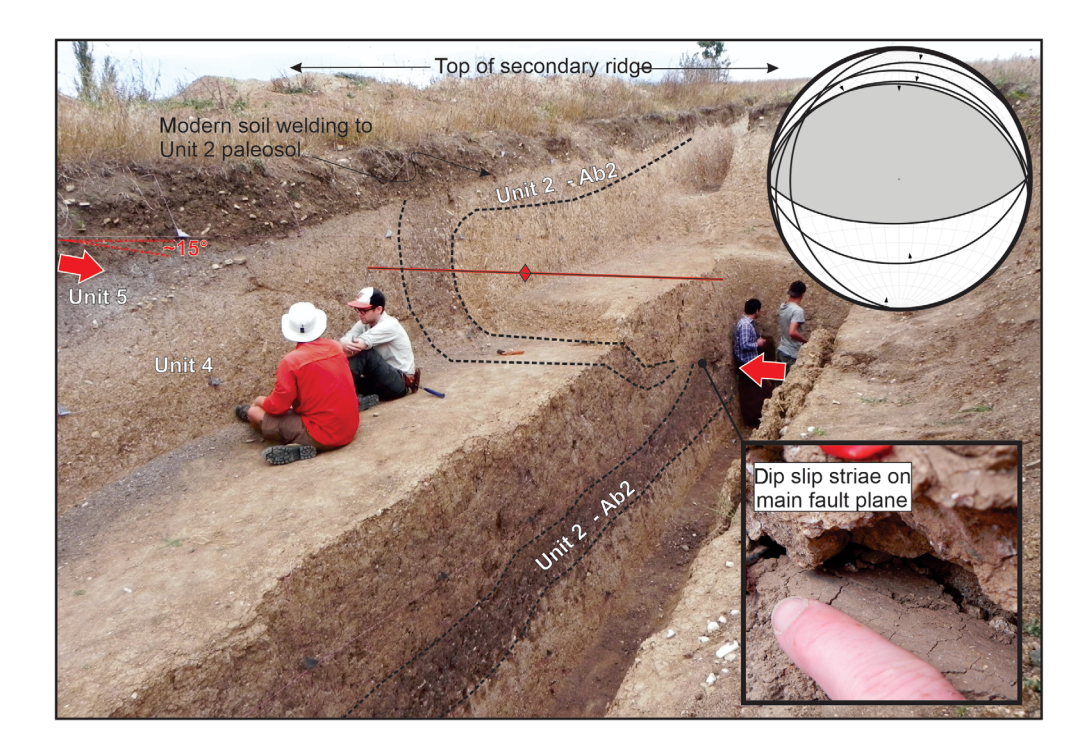


Figure 4. Field photographs of the fold, faults, and striae as exposed in the trench looking north—northwest and showing the western wall of the trench. The dashed lines delineate the upper and lower margins of the buried A horizon on unit 2 (Table S1). The red arrows point along the main thrust fault; the red line with diamond indicates approximate axial trace of overturned anticline in hanging wall of the thrust. Inset lower-hemisphere projection showing fault planes (great circles) and striae (arrows pointing in the direction of slip and indicating the motion of the hanging wall block relative to the footwall) measured in the trench; north-dipping planes are the main thrust and secondary synthetic faults, south-dipping planes are antithetic faults. The gray field indicates the best-fit moment tensor fault-plane solution using FaultKin8 (Marrett and Allmendinger, 1990). The color version of this figure is available only in the electronic edition.

Unit 4 is a silty clay with $\sim 10\%$ subangular to rounded clasts with an average diameter of 2–3 cm and a maximum of 7 cm. The unit tapers in thickness northward to where it onlaps unit 3 (undiff.). We interpret unit 4 to be fault scarp-derived colluvium.

Unit 5 is a lens of silty clay that is only present on the down-thrown side of the fault. It is distinguished from the underlying unit 4 by higher organic content and dark-gray color, diffuse and powdery CaCO₃ (as opposed to nodular), and a distinct stone line at its base. We interpret unit 5 to be a disturbed horizon, possibly from human activity or tree throw.

Unit 6 is the modern A horizon and comprises a laterally continuous layer of silty clay that is 0.5–0.75 m thick at the top of the trench. Clasts within the unit are randomly oriented, which we interpret to result from recent agricultural tilling.

Observed stratigraphic offsets and striated fault planes exposed within the trench indicate that a thrust fault dips $\sim 15^{\circ}-20^{\circ}$ at the base of the trench ($\sim M12H-2.5$ V, Fig. 3) and splays upward to the surface into a series of shallowly dipping synthetic and antithetic faults (Figs. 3, 4). Fault planes are striated with orientations indicating predominantly dip-slip

motion (Fig. 4). Short antithetic faults with centimeter-scale displacements are likely related to displacement on the master fault and the development of a tight (~3 m wavelength), overturned fault-propagation fold (Fig. 4). Deposits and soil horizons thicken into the hinge zone of the fold. We interpret that fault splays have broken through the fold over and through younger depositional trench units.

Interpreted event chronology

Trench logging revealed structural and soil-stratigraphic relationships indicating evidence for a minimum of four surface-deforming ruptures. We first present the evidence for these events numbered in chronological order and then describe reconstruction of single-event displacements (SEDs) in the section that follows.

There is evidence for a minimum of one event, and likely many more, prior to

deposition of unit 1. This is indicated by the subvertical beds of unit 0 on the hanging wall (M16-24 H, Fig. 3), which are interpreted to be the oldest deposits in the trench. As seen earlier, we infer unit 0 was deposited as a mixed colluvialalluvial apron where the Lekhura River emanates from the Black Forest anticline (Fig. 2). Because of their position in the landscape, it is possible that beds of unit 0 were folded within the forelimb zone of the larger anticline (Fig. 2) prior to modification and subsequent basinward (i.e., south of the antecedent fold) deposition of unit 1. There may have been displacement on the main thrust exposed in the trench during this time, but we did not observe evidence to test this hypothesis. Despite the uncertainties in the earliest depositional and deformational history, it is clear that after the majority of unit 0 tilting, a new ground surface developed over an eroded unit 0, followed by the deposition of unit 1 and then development of soil profile unit 2. This ground surface was likely stable for a prolonged period and prior to faulting and folding of units 1 and 2, based on both the thickness of the soil profile (\sim 1.5 m) and the well-developed B horizon in unit 2 (e.g., Tonkin and Basher, 1990).

Event E1 is interpreted to have folded units 1 and 2 and produced a fold scarp with no surface rupture, —that is, unit 2 was not thrust over the paleoground surface. Erosion of the hanging wall began thinning unit 2 and contributed to the deposition of unit 3 in the footwall. We infer that unit 3a, a buried A horizon, developed after an initial period of scarp modification and erosion, when the rate of soil formation exceeded the rate of deposition in the footwall. It is unclear whether unit 3a originally extended across the fold and into the hanging wall.

Event E2 is marked by thrusting of unit 2 over unit 3 along the main fault and folding of the contact between units 2 and 3 (undiff.). We interpret the fault to have broken through the pre-existing fold scarp to the ground surface in this event, and a shallow splay of the main fault overrode the ground surface along the top of unit 3a, displacing units 1–3 and folding the base of unit 3 (undiff.) in the hinge of the anticline. An antithetic thrust was active in the footwall, displacing unit 3 but dying out down-dip in the trench wall (Fig. 3). After event 2, erosion of the up-thrown side of the scarp possibly renewed deposition near the top of unit 3 (undiff.) via erosion of units 1–2 (and possibly 3a) in the hanging wall, ultimately resulting in the deposition of unit 4 as a new unit in the footwall. Following deposition of unit 4, unit 5 was created by human modification or tree throw at or near ground level.

Event E3 (most recent event [MRE]) is indicated by discrete displacement of the contact between units 4 and 5 along a single fault strand (inset, Fig. 3; see the supplemental material for high-resolution orthophoto) that can be traced down the trench wall to the main thrust. Other small displacements of the contact between units 4 and 3 (undiff.) also occurred during E3 along two other fault splays beneath this main fault. It is possible that E3 displaced the ground surface, but there is no discrete fault scarp at the site and the contact between unit 5 and the modern topsoil (unit 6) is not visibly deformed.

Trench reconstruction for events E3 through E1

Here, we present observed and restored displacements of the earlier events from youngest to oldest to sequentially restore the deformation (Fig. 5). Ranges in measured displacements reflect our estimated uncertainty based on measuring on-fault, dip-slip separations of key horizons on the trench wall. This approach accounts for folding by restoring the throw indicated by displaced horizons outside of the hanging wall anticline.

The displaced contacts between (1) units 5 and 4 and (2) units 4 and 3 (undiff.) are 5 cm and a cumulative 30.5 ± 5.5 cm, respectively, across two fault strands that merge at depth. As we interpret these displacements to have all occurred in E3, the up-dip decrease in slip implies die out of displacement toward the surface, which could have been accommodated in the broader fold (Figs. 3, 4). The older contact between units 3 (undiff.) and 2 is displaced 42.5 ± 1.5 cm along the same fault strand, providing a maximum bound on the slip during E3 under an end-member scenario in which none of the offset

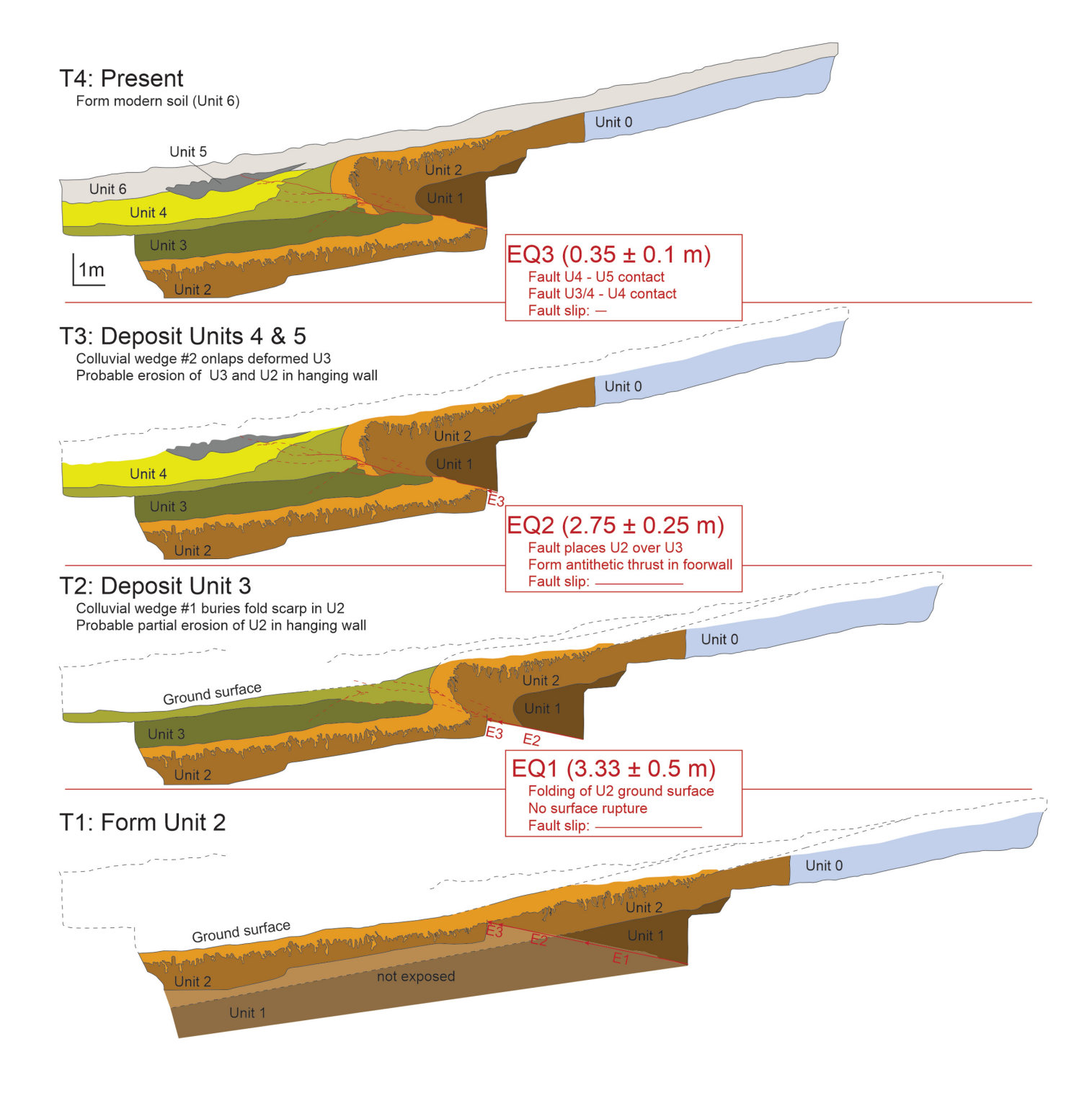
of this lower contact occurred during a prior event E2. Consistent with the small offset (\sim 5 cm) of the shallowest contact, there is no colluvial wedge associated with E3, although the thickness of the modern soil (unit 6) increases downslope of the fault in which some additional material has accumulated. We therefore adopt a displacement of 35 cm and conservative uncertainty estimate of \pm 10 cm for E3 (Fig. 5). For this and other estimates of SEDs, we consider all values within the range to be equally likely (i.e., 35 \pm 10 cm indicates that all values in the range 25–45 cm are equally likely).

Epistemic uncertainties in displacement measurements increase with older events, as they depend on where one places the contact between units 3 and 4, which is indistinct near the top of unit 3 (undiff). In our measurement of E2 and E3 displacements, we make the following simplifying assumptions: (1) that unit 3 (undiff.) is entirely composed of unit 3, which is near-vertical in the hinge zone of the fold (Fig. 5), (2) that the base of unit 3 (undiff.) in the hanging wall restores to the base of unit 3 in the footwall, and (3) that the maximum displacement for E3 of 42.5 ± 1.5 cm (from offset of the unit 3 (undiff.) and unit 2 contact) occurred entirely in E3. We consider these assumptions to be reasonable considering that the stratigraphic thickness of unit 3 (undiff.) is roughly the same as the combined thickness of units 3 and 3a, and that a minimum of ~30 cm of slip is required just ~1 m up-dip from the maximum displacement measurement for E3. Restoring the basal contact between unit 3 (undiff.) and unit 2 on the main fault strand, and accounting for 42.5 \pm 1.5 cm displacement in E3, yields a displacement of 2.75 m for event E2 (Fig. 5). We adopt a conservative estimate of uncertainty for this measurement of \pm 0.25 m.

The estimation of slip in event E1 depends on (1) the reconstructed slope of the pre-E2 ground surface, represented by the dip of unit 2 and (2) the locations of the resulting hanging wall and footwall cutoffs. For our reconstruction, we used the boundary between the buried A and B horizons in unit 2, because this was easily traced in the field. There is little uncertainty in the slope of this boundary in the footwall, and the resulting bed-fault intersection is 20°. We consider the slope of the boundary on the hanging wall to lie between two end member values, resulting in horizon-fault intersection angles between \sim 20° (when the boundary on the hanging wall is parallel to that of the footwall) and \sim 27° (boundary on the hanging wall is steeper than that of the footwall). Restoring the horizon boundary with E1 slip requires 3.81 or 2.85 m of slip for those two scenarios, respectively. We therefore assign a preferred slip value for E1 of 3.33 \pm 0.50 to incorporate the range of measurements (Fig. 5). The cumulative slip along this fault in three events is thus 6.53 ± 0.85 m.

Radiocarbon dates and unit ages

We collected seven gastropods embedded in trench stratigraphy to constrain the ages of units and events (Fig. 6). We also collected four modern snail shells to constrain fraction modern

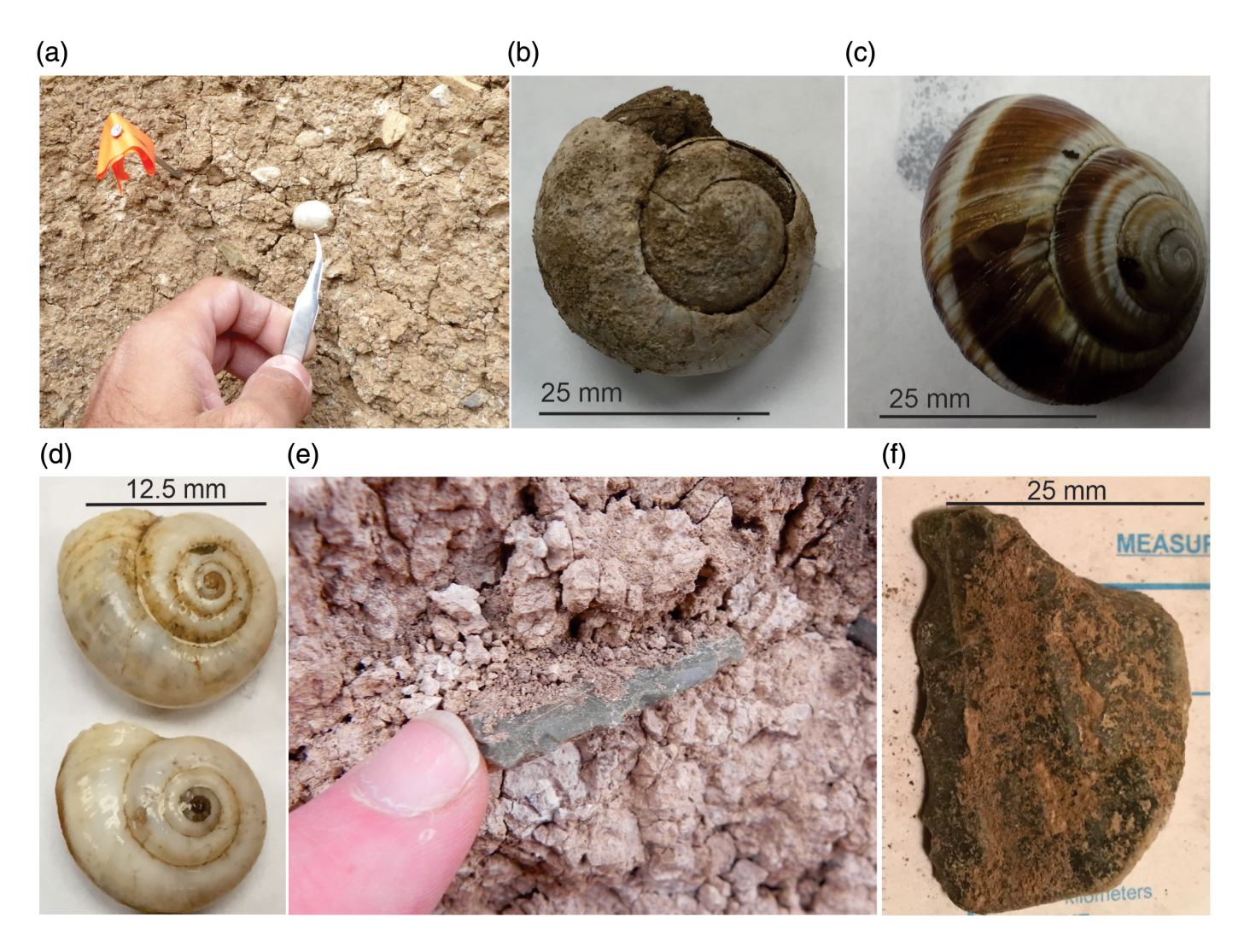


 (F_M) of the two species and three bulk soil samples for charcoal extraction and dating.

Our gastropod samples have F_M values of 0.8119–0.9548, meaning they contain about 5%–19% old carbon, which results in 14 C dates of 370–1675 yr for the modern samples. Samples of H. lucorum yielded lower values of old carbon (dates of 370–645 yr or 5% and 8% old carbon) than did X. derbentina (920–1675 yr, or 11% and 19% old carbon; Table 1). To correct the dates of the ancient samples, we subtract from the measured radiocarbon date the mean value for the radiocarbon date anomaly (Goodfriend and Ellis, 2000) of 508 \pm 138 or

Figure 5. Sequential trench reconstruction from present (time T4) to pre-EQ1 (T1). The amount of fault slip in each time step is depicted by the length of red lines (with scale established in top panel). See Trench Reconstruction for Events E3 through E1 section for discussion of assumptions, slip measurements, and assigned uncertainties.

 1298 ± 378 ¹⁴C yr for *H. lucorum* and *X. derbentina*, respectively. Uncertainties include both analytical error and error in the age anomaly correction (after Goodfriend and Ellis, 2000). We then use the corrected conventional radiocarbon date and uncertainty to determine the calibrated ages listed in Table 1.



Future studies are needed to obtain a more systematic characterization of age anomalies in these two species as well as the potential for postburial open-system behavior (e.g., Pigati *et al.*, 2010; Rech *et al.*, 2011; see the supplemental material for more discussion).

We obtained charcoal from bulk soil samples of units 5, 4, and 3 for comparison with the gastropod dates. Unit 5 yielded fine-grained fragments of charcoal from unidentified hardwood, whereas units 3 and 4 only yielded microcharcoal fragments. Charcoal extraction was attempted on unit 1, but not enough material was recovered for AMS dating. Rootlets, snail shells, and periderm fragments were common in all samples, and a small amount of seed was recovered from unit 4.

The age of unit 1 is constrained by a single date on a fragment of H. lucorum at 44,580–47,530 cal B.P. (2σ) (Sample U1-S7, Table 1). Because this age approaches the practical limits of radiocarbon dating, we treat this as a minimum bound on the ages of units 1 and 0.

The age of unit 2 is constrained by a single date on a fragment of *H. lucorum* at 42,459–44,159 cal B.P. (Sample U2-S8, Table 1), which is in stratigraphic order with the minimum age of unit 1 and conforms to our interpretation of unit 2 as a soil

Figure 6. Photographs of samples and sampling targets at the trench site. (a) Field photograph of *H. lucorum* snail shell encased in sediment (unit 1) and (b) a laboratory photograph of a nearly intact *H. lucorum* shell from the same unit. (c) Laboratory photograph of a modern *H. lucorum* shell collected from the modern ground surface. (d) Laboratory photograph of *X. derbentina* shells taken from the modern ground surface. (e) Field photograph of a denticulate stone tool found within the buried paleosol unit 2. (f) Laboratory photograph of profile view of the stone tool showing the shape of serrations (left edge) and chips used to form them. The color version of this figure is available only in the electronic edition.

developed in unit 1. However, we again treat this date as a minimum bound on the age of unit 2 because it, too, approaches the practical limit of radiocarbon dating. Further inspection of the denticulate stone from unit 2 (Fig. 6) confirmed that it is likely a Paleolithic age (>10–12 ka) artifact used for cutting (Robert Whallon, personal comm., 2017), which is consistent with the >40 cal ka B.P. age of unit 2. Humans have been in the northern Caucasus region for at least ~33 ka (Bar-Yosef *et al.*, 2011) and tool-crafting hominins for significantly longer (Lordkipanidze *et al.*, 2013).

TABLE 1 Sample Catalog	TABLE 1 Sample Catalog, ¹⁴ C Accelerator Mass Sp	ectrometry	Spectrometry (AMS) Laboratory Results, and Age Calibrations	Age Calibra	tions					
		Laboratory		Fraction		Conventional	+1	Corrected	+1	U
Field Code	Location on Log	Code	Species or Sample Type	Modern	\pm (10)	¹⁴ C Age	(1σ)	¹⁴ C Age*	$(1\sigma)^{\dagger}$	$\overline{}$
Okami 001	N/A, collected from surface	218724	H. lucorum	0.9548	0.0019	370	20	1	ı	- 1
Okami 002	N/A, collected from surface	218725	H. lucorum	0.9226	0.0018	645	20	I	1	- 1
Okami 004a	N/A, collected from surface	218726	X. derbentina	0.8919	0.0017	920	15	I	1	- 1
Okami 004b	N/A, collected from surface	218727	X. derbentina	0.8119	0.0016	1,675	20	I	ı	- 1
U5-S12	M4.02 H-3.53 V	178925	H. lucorum	0.6057	0.0010	4,025	15	3,517	138	Μ
U4-S10	M4.52 H-3.07 V	178924	Fragment—likely H. Iucorum	0.0455	0.0005	24,820	90	24,312	164	7
U4-S15	M6.83 H-3.84 V	218728	H. lucorum	0.0137	0.0004	34,460	270	33,952	303	Μ
U3a-S11	M7.59 H-2.83 V	178923	Fragment—likely X. derbentina	0.0111	0.0004	36,150	320	34,852	494	Μ
U3-P9	M6.22 H-1.83 V	178922	Fragment—likely H. Iucorum	0.0128	0.0004	35,040	270	34,532	303	Μ
U2-S8	M8.78 H-1.58 V	178921	Fragment—likely H. Iucorum	0.0070	0.0004	39,910	490	39,402	509	4
U1-S7	M12.98 H-3.20 V	178920	Fragment— <i>H. lucorum</i>	0.0047	0.0004	43,040	720	42,532	733	4
Unit 5-M5.5-3.5	M5.50 H-3.5 V	PRI-5659	Hardwood charcoal fragments	ı	ı	2,040	22	N/A	N/A	_
			from bulk soil sample							
Unit 4-M5.5-2.75	M5.50 H-2.75 V	PRI-5660	Microcharcoal	I	I	38,899	170	N/A	N/A	4
Unit 3-M6.8-1.8	M6.8 H-1.80 V	PRI-5661	Microcharcoal	ı	1	48,354	403	NA	N/A	4

27,950-28,714 37,486-39,198 38,437-40,558 38,454-39,768 42,459-44,159 44,580-47,530

3,455-4,219

42,480-43,100 47,580-49,210

1,920-2,110

Calibrated Age Range (Years B.P.) (2 σ) Sample locations are also indicated in Figure 3, and coordinates are given relative to an origin of MOH-0 V in the lower south corner of the trench. Examples of sample targets are shown in Figure 6. olach (1977), with $\delta^{13}C$ values measured on prepared graphite using the AMS spectrometer. These can differ from differ from differ from disconding material, if fractionation occurred during sample graphitization or the AMS measurement, and are not shown. All calibrations conducted with IntCal13 curves (Reimer et al., 2013) on OxCal v.4.3.2 (Bronk-Ramsey, 2017).

*The corrected conventional radiocarbon age is simply the conventional radiocarbon age of the sample minus the mean age of the mean age of the modern sample for that species (Goodfriend and Ellis, 2000)

The 1σ errors are calculated by summing in quadrature the 1σ uncertainty of the species-specific age correction and the 1σ uncertainty of the conventional radiocarbon age for that sample (Goodfriend and Ellis, 2000).

The ages of units 3 and 3a are constrained by single-fossil shell dates of 38,454–39,768 (Sample U3-P9) and 38,437–40,558 cal B.P. (Sample U3a-S11, Table 1), respectively. The two dates significantly overlap, as one might expect for a colluvial unit (unit 3) overlain by a weakly developed soil (unit 3a). In unit 3, bulk-soil microcharcoal returned an age of 47,580–49,210 cal B.P. (sample unit 3-M6.8-1.8, Table 1), which we interpret to result from recycling of older charcoal in units 1 and 2. Because unit 3 is interpreted to have formed against a fold scarp (Fig. 5), it may contain older material from units 1 or 2, including fossil shells. In the absence of additional information for this unit, and constrained by bounding units, we accept the ~38–40 ka age for units 3 and 3a.

Determining the age of unit 4 is complicated by two issues. First, the dates from the two fossil shells are not in stratigraphic order, with the stratigraphically deeper sample U4-S10 returning a date of 27,950–28,714 cal B.P. and the overlying sample U4-S15 yielding an older and nonoverlapping date of 37,486–39,198 cal B.P. Second, the microcharcoal age is 42,480–43,100 cal B.P. (sample unit 4-M5.5-2.75, Table 1), which is significantly older than both gastropod samples. The lack of repeatability of these measurements between and within sample targets is a concern and could result from a number of different factors, including U4-S15 being derived in part from older material (see the supplemental material). Because stratigraphic relations indicate unit 4 is younger than unit 3, we tentatively assign unit 4 a minimum age of 27,950–28,714 cal B.P., based on sample U4-S10, and reject the two older ages.

Unit 5: AMS dating of 27 hardwood charcoal fragments (7 mg) from unit 5 returned a date of 1920–2110 cal B.P. (sample unit 5-5.5-3.5, Table 1), which is \sim 1500–2000 yr younger than the anomaly corrected and calibrated date of 3455–4219 cal B.P. from the fossil shell within the same unit (Sample U5-S12, Table 1). This discrepancy could result from introduction of younger hardwood charcoal fragments via bioturbation or in situ burning, both of which are consistent with our interpretation of unit 5 forming via human activity or tree throw. To account for the range of ages, we adopt a conservative age range of 1920–4219 cal B.P. (i.e., 3070 \pm 1150, with uniformly distributed age uncertainties) for unit 5.

In summary, consideration of all of the dates together with stratigraphic relations indicated by the trench log (Figs. 3, 5) leads to the following:

- 1. Within 2σ uncertainty, the fossil shell dates are in stratigraphic order throughout the trench, except for inconsistency between the two samples within unit 4 (U4-S10 and U4-S15).
- 2. Dates from fossil shells and microcharcoal follow stratigraphic ordering of units but do not overlap within error. In unit 5, the shell ages are older than the charcoal, whereas in units 4 and 3 the disparity is larger and in the opposite sense.

3. These inconsistencies can be explained by redeposition of material eroded from hanging wall units, such as shell U4-S15, which is nearest the fold axis, or recycling of the microcharcoal in units 3 and 4. Likewise, addition of younger charcoal to unit 5 is consistent with the noncolluvial and potentially anthropogenically modified nature of this deposit.

On the weight of these factors, and assuming no open system behavior of fossil shells, we prefer the fossil shell ages for units 1–3a, the younger shell age for unit 4, and a combined age for unit 5. However, we acknowledge that there are inherent uncertainties in the ages of units 1–5 that we are unable to fully resolve in this study.

DISCUSSION

Earthquake chronology

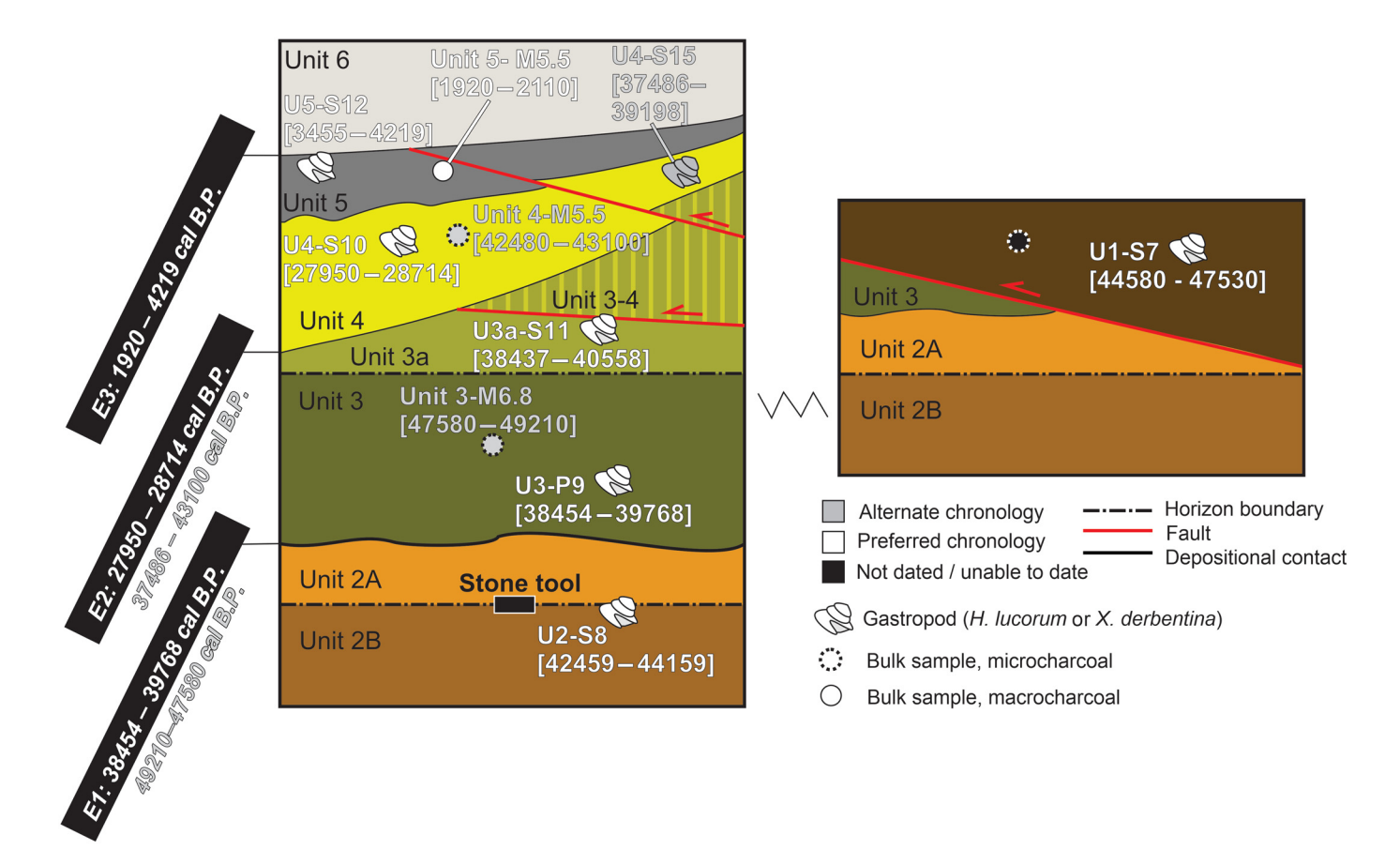
Our trench interpretations and radiocarbon dating allow us to identify three loosely dateable events (see Fig. 3 for log and sample locations and Fig. 7 for schematic and interpreted event ages based on dates). Because of the large epistemic uncertainties associated with all samples, we do not undertake Bayesian age modeling for the timing of the three events to avoid implying an undue level of confidence. Instead, we present two simple earthquake chronologies (Fig. 7).

In our preferred chronology, the antepenultimate earthquake E1 occurred between 38,454 and 39,768 cal B.P. (based on the age of unit 3 from shell U3-P9); the penultimate earthquake E2 occurred between 27,950 and 28,714 cal B.P. (age of unit 4 from U4-S10, under the assumption the other material is recycled older material); and the MRE E3 occurred between 1920 and 4219 cal B.P. (age of unit 5 from combination of charcoal and shell ages). Our preferred chronology (white text, Fig. 7) contains two closed recurrence intervals of ~11 ka (E1-E2) and ~25 ka (E2-E3), and a modern open interval of ~3000 yr (post E3).

In our alternative chronology, the antepenultimate earth-quake E1 occurred between 49,210 and 47,580 cal B.P. (age of unit 3 from microcharcoal 3-M6.8-1.8); the penultimate earthquake E2—occurred between 37,486 and 43,100 cal B.P. (age of unit 4 from microcharcoal 4-M5.5-2.75 combined with older fossil shell U4-S15); and the MRE E3 occurred between 1920 and 4219 cal B.P. (age of unit 5 from combination of charcoal and shell ages).

The alternative chronology (gray text, Fig. 7) also contains two closed recurrence intervals, with a shorter first interval of \sim 8 ka (E1–E2), a longer second interval of 35 ka (E2–E3), and the same modern open interval of \sim 3000 yr. As demonstrated subsequently, the choice of chronology does not significantly impact overarching interpretations regarding fault behavior.

The three events observed in the trench allow us to assess the incremental and time-averaged slip rates for the Okami thrust. Using a Monte Carlo method (see Data and Resources), we fit piecewise slip-time histories based on



observed SEDs, event ages, and uncertainties therein. Results from two models are shown in Table 2 and Figure 8, based on inputs from the preferred and alternative event chronologies (Fig. 7). In our preferred model, the mean slip rate was about $0.35 \text{ mm yr}^{-1} \text{ from } \sim 40 \text{ to } 28 \text{ ka and } 0.1 \text{ mm yr}^{-1} \text{ thereafter.}$ In the alternative model, the mean slip rate was about 0.58 mm yr⁻¹ from 48 to 40 ka and 0.08 mm yr⁻¹ thereafter. In an absolute sense, and for the purposes of seismic hazard, the differences in slip rate are relatively small, particularly considering epistemic uncertainty in how the radiocarbon dates represent the true ages of the units. However, the results show that regardless of the age model used, the slip rate was roughly $3-7\times$ higher in the interval between E1 and E2 than E2 and E3. This apparent slip-rate variability could be attributable to variability in both the SEDs and the long interval of quiescence (i.e., lack of surface rupture) between the penultimate event and MRE. In a global context, this rate change would be among the highest documented (Weldon et al., 2004; Zinke et al., 2017), but we stress that better age control, a longer record, and data from the other fault splays (Fig. 2) are required to support such a claim. In the following section we discuss our interpretation of the significance of this behavior.

Earthquake behavior

SEDs on the Okami thrust range from \sim 0.35 to >3 m (Figs. 7, 8). These SEDs are near-surface offsets of trench stratigraphy and therefore may be close enough to the surface for

Figure 7. Summary diagram depicting schematic stratigraphic and structural relationships as well as samples in the Okami trench. Sample names are the field codes reported in Table 1 with abbreviated bulk sample names. The white colors are ages used in our preferred chronology, whereas gray colors are ages used in the alternative chronology discussed in the Earthquake Chronology section. The black colors are samples that were not dated. Dates in brackets are all calibrated years before the present 2σ . The stratigraphic positions and interpreted ages of earthquakes E1–E3 are shown on the side of the diagram.

magnitude estimation using empirical scaling laws of surface rupturing events. Estimates of $M_{\rm w}$ from a single point along a fault are fraught with assumptions (e.g., Biasi and Weldon, 2006), especially considering that the Okami thrust we trenched is likely a splay from a larger fault system (e.g., Ritz et al., 2012). However, it is valuable to calculate a rough range of $M_{\rm w}$ values, considering the proximity of the fault to Tbilisi, the lack of similar studies elsewhere in the region, and the perception that most strain in the Caucasus is absorbed aseismically (Jackson, 1992). For example, assuming that displacements at this site were an average for the whole fault system, then the minimum and maximum SEDs we observe yield $M_{\rm w}$ estimates of 6.5–7.5, respectively, whereas treating the SEDs as maximum values for the fault system yields $M_{\rm w}$ estimates of 6.2-7.1 (all calculated using Wells and Coppersmith, 1994). The upper range of these estimates is consistent with the characteristic magnitudes for nearby active seismic sources ($\sim M_{\rm w}$ 7.5) presented in Onur et al. (2020).

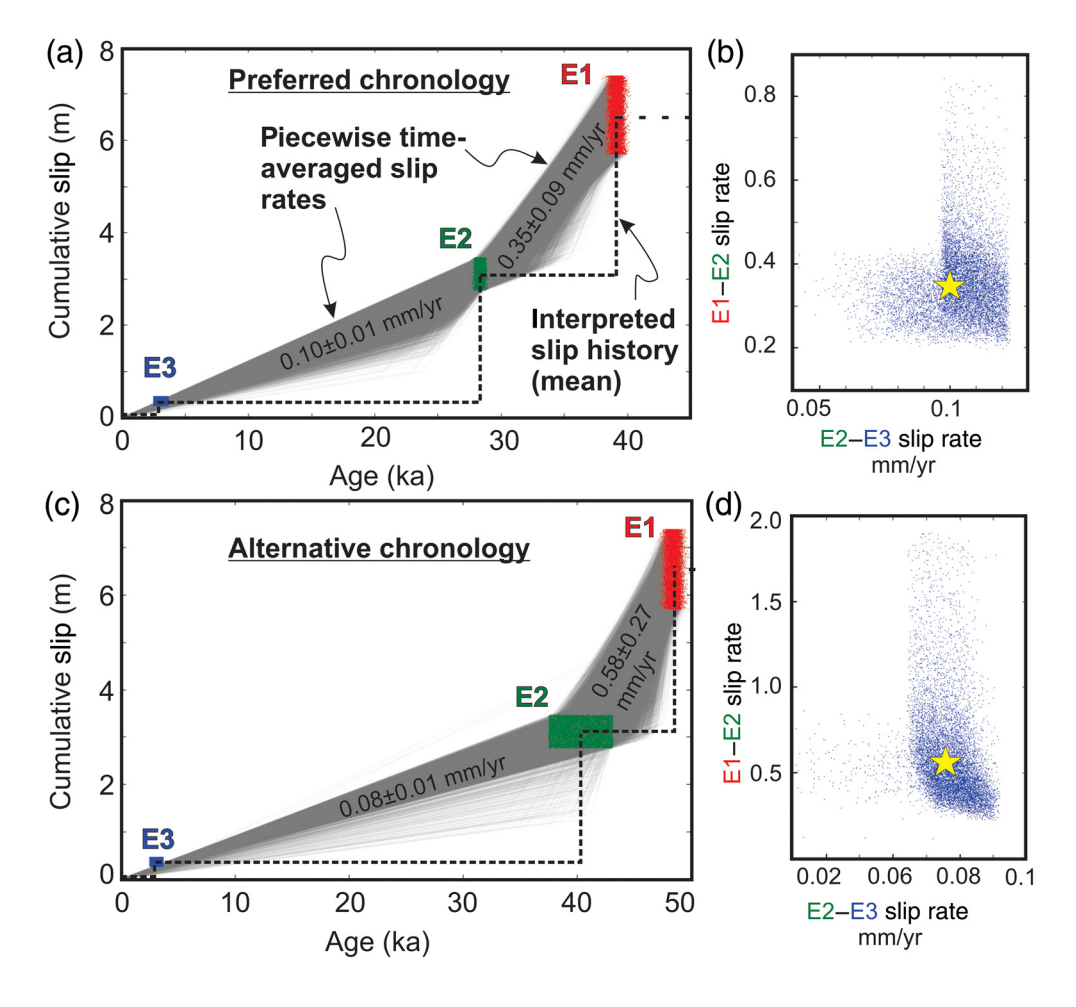


Figure 8. Time-averaged slip rate histories fit to known event ages and single-event displacements found in the trench. (a) Piecewise slip rates of ~0.1 and ~0.35 mm/yr are estimated for two closed seismic cycles in our preferred chronology (Table 2). The dashed line is the time-slip history interpreted from the trench, whereas gray lines are individual model runs using a Monte Carlo approach (see Data and Resources). The results from the model runs in panel (a) are plotted as blue dots in panel (b), with the yellow start indicating the position of the mean slip rate for both intervals. Panels (c) and (d) are correlative plots for the alternative chronology discussed in the Earthquake Chronology section. See Table 2 for model parameters and outputs. The color version of this figure is available only in the electronic edition.

The fault in this trench has an unusual rupture history. Acknowledging that our data come from just two full seismic cycles on a fault splay, our results point toward either a random relationship between slip and time or toward the exact opposite of time- and slip-predictable models (e.g., Shimazaki and Nakata, 1980). For instance, the earthquake interval between E1 and E2 was 50% shorter than the other (E2–E3) but produced roughly an order of magnitude more slip on the fault. There are several interrelated factors that might cause this behavior: (1) the Okami thrust is variably active in earthquakes nucleating on the underlying master fault, and therefore the amount of near-surface slip on this splay can vary between events with no slip deficit down-dip; (2) the way in which slip is distributed on this splay changes, so that apparently small on-fault slip is compensated by large off-fault folding in some

events; and/or (3) multifault earthquakes rupture to the surface via a complex network of low-angle thrusts at the surface (a common occurrence in thrust and reverse systems; Rubin, 1996), and the resulting surface rupture lengths and slip distributions for this fault vary from event to event. Without further study of the Black Forest ridge and surrounding structures, we cannot say what the relative influences of these factors are; however, all of these mechanisms could explain the variability in earthquake behavior.

Implications for seismic hazard in Georgia

The Okami trench site provides unequivocal paleoseismic evidence for surface rupturing earthquakes having occurred in the Greater Caucasus. The region has, however, experidamaging historical earthquakes with characteristics and magnitudes on par with the observations presented in this study. The 1991 $M_{\rm w}$ Racha earthquake ruptured an ~40°-dipping east-west-striking thrust fault and resulted in the deaths of 120 people but did not produce an identifiable surface rupture (Jibson et al., 1994; Fuenzalida et al.,

1997). No surface rupture was reported for a $M_{\rm s}$ 6.7 aftershock on a similarly oriented thrust fault ~100 km to the east the following year (Triep *et al.*, 1995). In 1920, the $M_{\rm s}$ 6.2 Gori earthquake (approximately 30 km west of the Okami trench site) resulted in the deaths of over 100 people but had no obvious surface rupture (Kondorskaya and Shebalin, 1982). More recently in 2009, an $M_{\rm e}$ 5.6 (see Data and Resources) earthquake ruptured a blind thrust in the region of the 1991 Racha event (Nikolaeva and Walter, 2016).

One outcome of this study is that it highlights the challenge of identifying surface rupturing faults and conducting seismic source characterization in the region. We were fortunate to uncover a three-event snapshot of a recently emergent, surface-rupturing thrust fault, as this confirms the potential value of future detailed mapping and paleoseismic investigations

 $0.267 (1\sigma)$ 0.579 ± 0.077 ± **Earthquake** E1-E2 E2-E3 Age Uncertainty 2.807 (uniform) 1.115 (uniform) $0.815(2\sigma)$ Age (ka), Alternative Chronology 40.293 3.070 $0.085(1\sigma)$ $0.012 (1\sigma)$ 0.352 ± 0.103 ± **Earthquake** E1-E2 E2-E3 Input Data Used to Calculate Slip Rates and Closed Interval Slip Rate Outputs Age Uncertainty 1.115 (uniform) $0.658 (2\sigma)$ 0.382 (2σ) Age (ka), Preferred Chronology 39.111 28.332 3.070 Slip Uncertainty 0.50 0.25 0.1 3.33 0.35 Ξ Earthquake 8

See Figure 7 for schematic diagram of trench chronology

around the Greater Caucasus. The utility of any other site will obviously depend on the availability of dateable material, relationships to major structures at depth, and how age data are treated; further radiocarbon analysis of modern terrestrial gastropod species and independent age controls will improve prospects for detailed geochronology.

This study also provides a glimpse of how relatively minor faults contribute to convergence over paleoseismic time-scales. If GPS convergence rates have remained somewhat steady through time, the Okami thrust—a short, frontal splay of an assumed master fault at depth (Fig. 2)—has accommodated just a small percentage (likely <10%) of the >3 mm yr⁻¹ shortening across the central Greater Caucasus (Sokhadze *et al.*, 2018). Although it is probable that the structure underlying the adjacent Black Forest anticline (Fig. 1) has a faster slip rate on par with faults farther to the west (Trexler *et al.*, 2020), and the cumulative shortening of these two structures could accommodate a non-negligible portion of the plate budget, the majority of geodetic strain remains unaccounted for in the geological record.

In 2002, the $M_{\rm s}\sim 4.5$ Tbilisi earthquake (Javakhishvili et al., 2004) caused ~100 building collapses and >8 deaths (Gamkrelidze et al., 2008). A shallow $M_{\rm w}$ 6–7 or greater earthquake on the Okami thrust could produce stronger ground motions and impacts on the city of Tbilisi and surrounding towns built along the fault system. If the Okami thrust is just part of a larger fault network as our data hints, the magnitude and impacts to these populations could be more severe.

CONCLUSIONS

A trench across a scarp in the foreland of the Greater Caucasus revealed evidence for recurrent surface rupturing earthquakes on a low-angle thrust fault. We documented three folding and faulting events over the last ~40 ka using detailed trench logging and restorations, as well as radiocarbon dating of abundant terrestrial gastropods. Observed time-varying slip rates of ~0.1-0.5 mm/yr and SEDs of \sim 0.3 to >3 m may be the result of local or regional fault interactions during rupture. Although the timing of specific events are only loosely constrained due to inherent uncertainties in unit ages, this study highlights that even minor active faults and folds in this region can accommodate potentially significant amounts of strain in the Caucasus orogen. Further characterization of active faults in Georgia, and particularly near the capital Tbilisi, will help improve estimates of seismic hazard in Georgia.

DATA AND RESOURCES

OxCal v.4.3.2 (Bronk-Ramsey, 2017) was used for all radiocarbon sample calibrations. We used the Styron (2015) Slip Rate Calculator v.0.1.4 to model piecewise slip rates from the event history (available via Zenodo, DOI: 10.5281/zenodo.1202048). Energy

magnitudes ($M_{\rm e}$) for historical earthquakes are those reported by the U.S. Geological Survey National Earthquake Information Center (USGS NEIC is available at https://earthquake.usgs.gov/earthquakes/search/). The supplemental material contains full unit descriptions and additional methodological considerations for dating samples from the trench. Figure S1 is an annotated orthophoto of the trench. The town locations and highway data provided in Figure 1 are from https://www.diva-gis.org/datadown. The population details provided in Figure 1 are from https://www.citypopulation.de/en/georgia/cities/ using data from the 11/5/2014. All websites were last accessed in April 2022.

DECLARATION OF COMPETING INTERESTS

The authors acknowledge that there are no conflicts of interest recorded.

ACKNOWLEDGMENTS

This article is based upon work supported by the National Science Foundation under Grant Numbers EAR 1451466 to T. A. S. and EAR 1524631 to E. C., which included support from the Office of International Science and Engineering. Chad Trexler conducted much of the structural mapping in the region, helped site the trench, and performed the Differential Global Positioning System (dGPS) survey of the scarp. This article benefited from reviews by Christoph Grützner, Jean-François Ritz, and Associate Editor Yann Klinger. The authors thank Levan Mumladze (Ilia State University) and Robert Whallon (University of Michigan) for assistance in identifying gastropods and archaeological samples, respectively. The authors are particularly grateful to the Georgian landowners, officials, and collaborators who helped ensure this work could take place: Ale Khachirashvili (landowner trench site), Zuniko Chaduneli (landowner, spoils pile), Gocha Gochitashvili (public official in Kaspi), Aleksander Karashvili (excavator), Dimitri Akubardia (magnetotelluric and shallow seismic surveys), Giorgi Ugrekhelidze (Global Positioning System [GPS] measurements), Luka Tsiskarishvili (total station survey), Kakha Surmava (driver), Irakli Skhirtladze (discussion of trench structure).

REFERENCES

- Abdullaev, R. N. (1962). *Geological Map of the USSR*, K-38-XXVIII, Ministry of Geology and Mineral Protection USSR, Moscow.
- Adamia, S., V. Alania, A. Chabukiani, G. Chichua, O. Enukidze, and N. Sadradze (2010). Evolution of the late Cenozoic basins of Georgia (SW Caucasus): A review, Geol. Soc. 340, 239–259.
- Adamia, S., V. Alania, N. Tsereteli, O. Varazanashvili, N. Sadradze, N. Lursmanashvili, and A. Gventsadze (2017). Postcollisional tectonics and seismicity of Georgia, in Tectonic Evolution, Collision, and Seismicity of Southwest Asia: In Honor of Manuel Berberian's Forty-Five Years of Research Contributions, R. Sorkhabi (Editor), Vol. 525, Geological Society of America Special Paper, Boulder, Colorado, 684 pp.
- Adamia, S. A., M. Lordkipanidze, and G. S. Zakariadze (1977). Evolution of an active continental margin as exemplified by the Alpine history of the Caucasus, *Tectonophysics* 40, nos. 3/4, 183–199.
- Alania, V., T. Beridze, O. Enukidze, R. Chagelishvili, Z. Lebanidze, D. Maqadze, A. Razmadze, N. Sadradze, and N. Tevzadze (2021). The geometry of the two orogens convergence and collision zones in

- central Georgia: New data from seismic reflection profiles, in *Building Knowledge for Geohazard Assessment and Management in the Caucasus and other Orogenic Regions*, F. L. Bonali, F. P. Mariotto, and N. Tsereteli (Editors), NATO Science for Peace and Security, Series C: Environmental Security, Springer, Dordrecht, 458 pp.
- Alania, V. M., A. O. Chabukiani, R. L. Chagelishvili, O. V. Enukidze, K. O. Gogrichiani, A. N. Razmadze, and N. S. Tsereteli (2017). Growth structures, piggy-back basins and growth strata of the Georgian part of the Kura foreland fold-thrust belt: Implications for late Alpine kinematic evolution, Geol. Soc. Lond. Spec. Publ. 428, 171–185.
- Argus, D. F., R. G. Gordon, M. B. Heflin, C. Ma, R. J. Eanes, P. Willis, W. R. Peltier, and S. E. Owen (2010). The angular velocities of the plates and the velocity of Earth's centre from space geodesy, *Geophys. J. Int.* 180, 913–960.
- Avdeev, B., and N. A. Niemi (2011). Rapid Pliocene exhumation of the central Greater Caucasus constrained by low-temperature thermochronometry, *Tectonics* **30**, TC2009, doi: 10.1029/2010TC002808.
- Banks, C. J., A. G. Robinson, and M. P. Williams (1997). Structure and regional tectonics of the Achara-Trialet fold belt and the adjacent Rioni and Karli foreland basins, Republic of Georgia, in *Regional and Petroleum Geology of the Black Sea and Surrounding Region*,
 A. G. Robinson (Editor), Vol. 68, American Association of Petroleum Geologists AAPG Memoir, Tulsa, Oklahoma, 331–346.
- Bar-Yosef, O., A. Belfer-Cohen, T. Mesheviliani, N. Jakeli, G. Bar-Oz,
 E. Boaretto, P. Goldberg, E. Kvavadze, and Z. Matskevich (2011).
 Dzudzuana: An upper Palaeolithic cave site in the Caucasus foothills (Georgia), *Antiquity* 85, 331–349.
- Biasi, G. P., and R. J. Weldon (2006). Estimating surface rupture length and magnitude of paleoearthquakes from point measurements of rupture displacement, *Bull. Seismol. Soc. Am.* **96**, 1612–1623
- Bronk-Ramsey, C. (2017). Methods for summarizing radiocarbon datasets, *Radiocarbon* **59**, 1809–1833.
- Cowgill, E., A. M. Forte, N. Niemi, B. Avdeev, A. Tye, C. Trexler, Z. Javakhishvili, M. Elashvili, and T. Godoladze (2016). Relict basin closure and crustal shortening budgets during continental collision: An example from Caucasus sediment provenance, *Tectonics* 35, 2918–2947.
- Cowgill, E., N. Niemi, A. Forte, and C. Trexler (2018). Reply to Comment by Vincent et al., *Tectonics* **37**, no. 3, 1017–1028, doi: 10.1002/2017TC004793.
- DeCelles, P. G. (2012). Foreland basin systems revisited: Variations in response to tectonic settings, in *Tectonics of Sedimentary Basins*: *Recent advances*, C. Busby and A. Azor (Editors), John Wiley, Hoboken, New Jersey, 405–426.
- Dotduyev, S. (1986). Nappe structure of the Greater Caucasus range, *Geotectonics* **20**, no. 5, 420–430.
- Forte, A. M., E. Cowgill, T. Bernardin, O. Kreylos, and B. Hamann (2010). Late Cenozoic deformation of the Kura fold-thrust belt, southern Greater Caucasus, *Geol. Soc. Am. Bull.* **122**, 465–486.
- Forte, A. M., E. Cowgill, I. Murtuzayev, T. Kangarli, and M. Stoica (2013). Structural geometries and magnitude of shortening in the eastern Kura fold-thrust belt, Azerbaijan: Implications for the development of the Greater Caucasus mountains, *Tectonics* 32, 688–717.

- Forte, A. M., E. Cowgill, and K. X. Whipple (2014). Transition from a singly vergent to doubly vergent wedge in a young orogen: The Greater Caucasus, *Tectonics* **33**, 2077–2101.
- Fuenzalida, H., L. Rivera, H. Haessler, D. Legrand, H. Philip, L. Dorbath, D. McCormack, S. Arefiev, C. Langer, and A. Cisternas (1997). Seismic source study of the Racha-Dzhava (Georgia) earthquake from aftershocks and broad-band teleseismic body-wave records: An example of active nappe tectonics, *Geophys. J. Int.* 130, 29–46, doi: 10.1111/j.1365-246X.1997.tb00985.x.
- Gamkrelidze, I. P. (1986). Geodynamic evolution of the Caucasus and adjacent areas in Alpine time, *Tectonophysics* **127**, no. 3, 261–277, doi: 10.1016/0040-1951(86)90064-8.
- Gamkrelidze, I., T. Tsamalashvili, E. Nikolaeva, T. Godoladze, Z. Djavakhishvili, and M. Elashvili (2008). Tbilisi fault and seismic activity of Tbilisi environs (Georgia), *Proc. A. Janelidze Geol. Inst.* 124, 30–35.
- Goodfriend, G. A. (1987). Radiocarbon age anomalies in shell carbonate of land snails from semi-arid areas, *Radiocarbon* **29**, 159–167.
- Goodfriend, G. A., and G. L. Ellis (2000). Stable carbon isotope record of Middle to Late Holocene climate changes from land snail shells at Hinds Cave, Texas, *Quat. Int.* **67**, 47–60.
- Goodfriend, G. A., and J. J. Stipp (1983). Limestone and the problem of radiocarbon dating of land-snail shell carbonate, *Geology* 11, 575-577.
- Gudjabidze, G. E. (2003). Geological Map of Georgia, 1:500,000, Georgian State Department of Geology and National Oil Company SAQNAVTOBI, Tbilisi, Georgia.
- Gunnels, M., G. Yetrimishli, S. Kazimova, and E. Sandvol (2020).
 Seismotectonic evidence for subduction beneath the eastern
 Greater Caucasus, Geophys. J. Int. 224, 1825–1834.
- Jackson, J. (1992). Partitioning of strike-slip and convergent motion between Eurasia and Arabia in eastern Turkey and the Caucasus, J. Geophys. Res. 97, 12,471–12,479.
- Javakhishvili, Z., T. Godoladze, M. Elashvili, T. Mukhadze, and I. Timchenko (2004). The Tbilisi earthquake of April 25, 2002 in the context of the seismic hazard of the Tbilisi urban area, *Boll. Geof. Teor. Appl.* 45, 169–185 (in Italian).
- Jibson, R. W., C. S. Prentice, B. A. Borissoff, E. A. Rogozhin, and C. J. Langer (1994). Some observations of landslides triggered by the 29 April 1991 Racha earthquake, Republic of Georgia, *Bull. Seismol. Soc. Am.* 84, 963–973.
- Khromovskikh, V. S., V. P. Solonenko, R. M. Semenov, and V. M. Zhilkin (1979). *Paleoseysmogeologiya Bolshogo Kavkaza* [Paleoseismogeology of the Greater Caucasus], Nauka Publ., Moscow, 188 pp. (in Russian).
- Kondorskaya, N. V., and N. V. Shebalin (1982). New Catalog of Strong Earthquakes in the USSR from Ancient Times Through 1977, Report SE-31, Translated and Published by World Data Center A for Solid Earth Geophysics, EDIS, Boulder, Colorado, 608 pp.
- Lordkipanidze, D., M. S. Ponce de León, A. Margvelashvili, Y. Rak, G. P. Rightmire, A. Vekua, and C. P. E. Zollikofer (2013). A complete skull from Dmanisi, Georgia, and the evolutionary biology of early *Homo*, *Science* 342, 326.
- Mamedov, A. V. (1973). *Geological Structure of the Mid-Kura Depression*, Elm, Baku, Azerbaijan, 194 pp. (in Russian).
- Marrett, R., and R. W. Allmendinger (1990). Kinematic analysis of fault-slip data, *J. Struct. Geol.* **12**, 973–986.

- McKenzie, D., J. Jackson, and K. Priestley (2019). Continental collisions and the origin of subcrustal continental earthquakes, *Can. J. Earth Sci.* **56**, 1101–1118, doi: 10.1139/cjes-2018-0289.
- Mellors, R. J., J. Jackson, S. Myers, R. Gok, K. Priestley, G. Yetirmishli, N. Turkelli, and T. Godoladze (2012). Deep earthquakes beneath the northern Caucasus: Evidence of active or recent subduction in western Asia, *Bull. Seismol. Soc. Am.* **102**, 862–866.
- Mumladze, T., A. M. Forte, E. S. Cowgill, C. C. Trexler, N. A. Niemi, M. Burak Yıkılmaz, and L. H. Kellogg (2015). Subducted, detached, and torn slabs beneath the Greater Caucasus, *GeoResJ* 5, 36–46.
- Nalivkin, D. V. (1976). Geologic Map of the Caucasus, Ministry of Geology, USSR.
- Nemčok, M., B. Glonti, A. Yukler, and B. Marton (2013). Development history of the foreland plate trapped between two converging orogens; Kura valley, Georgia, case study, Geol. Soc. Lond. Spec. Publ. 377, 159–188.
- Nikolaeva, E., and T. R. Walter (2016). InSAR observations of the 2009 Racha earthquake, Georgia, *Nat. Hazards Earth Syst. Sci.* **16,** 2137–2144.
- Onur, T., R. Gok, T. Godoladze, I. Gunia, G. Boichenko, A. Buzaladze, N. Tumanova, M. Dzmanashvili, L. Sukhishvili, Z. Javakishvili, et al. (2020). Probabilistic seismic hazard assessment using legacy data in Georgia, Seismol. Res. Lett. 91, 1500–1517.
- Pigati, J. S., J. Quade, T. M. Shahanan, and C. V. Haynes (2004). Radiocarbon dating of minute gastropods and new constraints on the timing of late Quaternary spring-discharge deposits in southern Arizona, USA, *Palaeogeogr. Palaeoclimatol. Palaeoecol.* 204, 33–45.
- Pigati, J. S., J. A. Rech, and J. C. Nekola (2010). Radiocarbon dating of small terrestrial gastropod shells in North America, *Quat. Geochronol.* 5, 519–532.
- Rech, J. A., J. S. Pigati, S. B. Lehmann, C. N. McGimpsey, D. A. Grimley, and J. C. Nekola (2011). Assessing open-system behavior of 14 C in terrestrial gastropod shells, *Radiocarbon* 53, 325–335.
- Reilinger, R., S. McClusky, P. Vernant, S. Lawrence, S. Ergintav, R. Cakmak, H. Ozener, F. Kadirov, I. Guliev, R. Stepanyan, *et al.* (2006). GPS constraints on continental deformation in the Africa-Arabia-Eurasia continental collision zone and implications for the dynamics of plate interactions, *J. Geophys. Res.* 111, no. B5, doi: 10.1029/2005JB004051.
- Reimer, P. J., E. Bard, A. Bayliss, J. W. Beck, P. G. Blackwell, C. Bronk Ramsey, C. E. Buck, H. Cheng, R. L. Edwards, M. Friedrich, *et al.* (2013). IntCal13 and Marine13 radiocarbon age calibration curves 0–50,000 years cal BP, *Radiocarbon* 55, 1869–1887.
- Ritz, J. F., N. S. Balescu, M. Lamothe, R. Salamati, A. Ghassemi, A. Shafei, M. Ghorashi, and A. Saidi (2012). Paleoearthquakes of the past 30,000 years along the north Tehran fault (Iran), J. Geophys. Res. 117, no. B6, doi: 10.1029/2012JB009147.
- Rogozhin, E. A., A. G. Gurbanov, A. V. Marakhanov, A. N. Ovsyuchenko, A. V. Spiridonov, and E. E. Burkanov (2004). Ancient earthquake dislocations in the area of Elbrus volcano, north Caucasus, *Rus. J. Earth Sci.* 6, no. 4, 293–309.
- Rogozhin, E. A., S. L. Yunga, A. V. Marakhanov, E. A. Ushanova, N. A. Dvoretskaya, and A. N. Ovsyuchenko (2002). Seismic and tectonic activity of faults on the south slope of the NW Caucasus, *Rus. J. Earth Sci.* **4,** 233–241.

- Rubin, C. M. (1996). Systematic underestimation of earthquake magnitudes from large intracontinental reverse faults: Historical ruptures break across segment boundaries, *Geology* 24, 989–992.
- Shimazaki, K., and T. Nakata (1980). Time-predictable recurrence model for large earthquakes, *Geophys. Res. Lett.* 7, 279–282.
- Shirinov, F. A., and Y. P. Bajenov (1962). *Geological Structure of the Southern Foothills of the Greater Caucasus*, Azerneshr, Baku, Azerbaijan, 189 pp. (in Russian).
- Sokhadze, G., M. Floyd, T. Godoladze, R. King, E. S. Cowgill, Z. Javakhishvili, G. Hahubia, and R. Reilinger (2018). Active convergence between the Lesser and Greater Caucasus in Georgia: Constraints on the tectonic evolution of the Lesser–Greater Caucasus continental collision, *Earth Planet. Sci. Lett.* 481, 154–161.
- Stuiver, M., and H. A. Polach (1977). Discussion reporting of 14C data, *Radiocarbon* **19**, 355–363.
- Styron, R. (2015). Slip rate calculator, doi: 10.5281/zenodo.33360.
- Tari, G., D. Vakhania, G. Tatishvili, V. Mikeladze, K. Gogritchiani, S. Vacharadze, J. Mayer, C. Sheya, W. Siedl, J. J. M. Banon, et al. (2018). Stratigraphy, structure and petroleum exploration play types of the Rioni basin, Georgia, Geol. Soc. Lond. Spec. Publ. 464, 403–438.
- Tibaldi, A., V. Alania, F. L. Bonali, O. Enukidze, N. Tsereteli, N. Kvavadze, and O. Varazanashvili (2017). Active inversion tectonics, simple shear folding and back-thrusting at Rioni basin, Georgia, J. Struct. Geol. 96, 35–53.
- Tibaldi, A., E. Russo, F. L. Bonali, V. Alania, A. Chabukiani, O. Enukidze, and N. Tsereteli (2017). 3-D anatomy of an active fault-propagation fold: A multidisciplinary case study from Tsaishi, western Caucasus (Georgia), *Tectonophysics* 717, 253–269.
- Tonkin, P. J., and L. R. Basher (1990). Soil-stratigraphic techniques in the study of soil and landform evolution across the southern Alps, New Zealand, *Geomorphology* **3**, 547–575.
- Trexler, C. C., E. Cowgill, N. A. Niemi, D. Vasey, and T. Godoladze (2022). Tectonostratigraphy and major structures of the Georgian Greater Caucasus: Implications for structural architecture, alongstrike continuity, and orogen evolution, *Geosphere* 18, 211–240, doi: 10.1130/GES02385.1.
- Trexler, C. C., E. Cowgill, J. Q. G. Spencer, and T. Godoladze (2020). Rate of active shortening across the southern thrust front of the Greater Caucasus in western Georgia from kinematic modeling

- of folded river terraces above a listric thrust, *Earth Planet. Sci. Lett.* **544**, 116362.
- Triep, E. G., G. A. Abers, A. L. Lerner-Lam, V. Mishatkin, N. Zakharchenko, and O. Starovoit (1995). Active thrust front of the Greater Caucasus: The April 29, 1991, Racha earthquake sequence and its tectonic implications, *J. Geophys. Res.* 100, 4011–4033.
- Tsereteli, N., A. Tibaldi, V. Alania, A. Gventsadse, O. Enukidze, O. Varazanashvili, and B. I. R. Müller (2016). Active tectonics of central-western Caucasus, Georgia, *Tectonophysics* **691**, 328–344.
- Tye, A. R., N. A. Niemi, R. T. Safarov, F. A. Kadirov, and G. R. Babayev. (2021). Sedimentary response to a collision orogeny recorded in detrital zircon provenance of Greater Caucasus foreland basin sediments, *Basin Res.* 33, 933–967, doi: 10.1111/bre.12499.
- Vasey, D. A., E. Cowgill, and K. M. Cooper (2021). A preliminary framework for magmatism in modern continental back-arc basins and its application to the Triassic-Jurassic tectonic evolution of the Caucasus, Geochem. Geophys. Geosys. 22, e2020GC009490.
- Vincent, S. J., A. Saintot, J. Mosar, A. I. Okay, and A. M. Nikishin (2018). Comment on Relict basin closure and crustal shortening budgets during continental collision: An example from caucasus sediment provenance by Cowgill et al. (2016), *Tectonics* 37, 1006–1016.
- Weldon, R., K. Scharer, T. Fumal, and G. Biasi (2004). Wrightwood and the earthquake cycle: What a long recurrence record tells us about how faults work, *GSA Today* **14**, 4–10.
- Wells, D. L., and K. J. Coppersmith (1994). New empirical relationships among magnitude, rupture length, rupture width, rupture area, and surface displacement, *Bull. Seismol. Soc. Am.* 84, 974–1002.
- Zinke, R., J. F. Dolan, E. J. Rhodes, R. Van Dissen, and C. P. McGuire (2017). Highly variable latest Pleistocene-Holocene incremental slip rates on the Awatere fault at Saxton River, South Island, New Zealand, revealed by Lidar mapping and luminescence dating, Geophys. Res. Lett. 44, 11,301–11,310.
- Zonenshain, L. P., and X. Le Pichon (1986). Deep basins of the Black Sea and Caspian Sea as remnants of Mesozoic back-arc basins, *Tectonophysics* **123**, no. 1, 181–211, doi: 10.1016/0040-1951(86) 90197-6.

Manuscript received 8 October 2021 Published online 22 April 2022